CUKUROVA UNIVERSITY
INSTITUTE OF NATURAL AND APPLIED SCIENCES

MSc THESIS

Examining the efficiency of the HGCAL of CMS experiment by using light quark jet data produced by the Monte Carlo method

Zohra AZIMI

Physics Department

September, 2023

TABLE OF CONTENTS

CUKUROVA UNIVERSITY
INSTITUTE OF NATURAL AND APPLIED SCIENCES

MSc THESIS

Examining the efficiency of the HGCAL of CMS experiment by using light quark jet data produced by the Monte Carlo method

Zohra AZIMI

Advisor: Prof. Dr. İsa DUMANOĞLU

Department of Physics

ABSTRACT

This thesis is dedicated to a comprehensive investigation of the efficiency of the High Granularity Calorimeter (HGCAL) by means of an in-depth analysis of the characteristic behaviors exhibited by light quark jets. To accomplish this, a rigorous examination of simulated data is undertaken, offering valuable insights into the performance of the HGCAL. Furthermore, in this study data taken from proton-proton collisions at the energy of $\sqrt{s} = 14$ TeV in the Compact Muon Solenoid (CMS) at the Large Hadron Collider (LHC) has been used. The integration of detector response and the meticulous dissection of energy profiles from these simulated collision events play a pivotal role in the evaluation and validation of the HGCAL's efficiency in a real-world context. Through this multifaceted approach, a comprehensive understanding of the HGCAL's capabilities and limitations is elucidated, contributing significantly to the advancements in particle physics and detector technology.

Keywords: Light quark jets, HGCAL, LHC, CMS.

ÇUKUROVA ÜNİVERSİTESİ
FEN BİLİMLERİ ENSTİTÜSÜ

YÜKSEK LİSANS TEZİ

Monte Carlo ile Üretilmiş Hafif KuarkJet Verilerini Kullanarak CMS'in HGCAL'in Verimliliğinin İncelenmesi

Zohra AZİMİ

Danışman: Prof. Dr. İsa DUMANOĞLU

Fizik Anabilim Dalı

ÖZ

Bu tez, hafif kuark jetlerinin karakteristik davranışlarını analiz etme yoluyla Yüksek Tanecikli Kalorimetrenin (HGCAL) verimliliğini araştırmaktadır. Bunun için HGCAL'ın performansına ilişkin bilgileri içeren , Monte Carlo (MC) simülasyon verileri incelenmiştir. Ayrıca bu çalışmada, Büyük Hadron Çarpıştırıcısı'ndaki (BHÇ) Compact Muon Solenoid (CMS) deneyinin sınırları içinde, $\sqrt{s} = 14\,\text{TeV}$ 'lik kütle merkezi enerjisinde simüle edilen proton-proton çarpışmalarından elde edilen veriler kullanılmıştır. HGCAL' nin verimliliğinin değerlendirilmesinde dedektör yanıtları ve enerji incelemeleri çok önemlidir. Bu yaklaşım sayesinde, HGCAL'in verimliliği ve sınırları hakkında kapsamlı bir açıklama ve parçacık fiziğinde kullanılan dedektör teknolojisindeki gelişmelere önemli ölçüde katkıda bulunması düşünülmektedir.

Anahtar Kelimeler: Hafif kuark jet, HGCAL, BHÇ, CMS

GENİŞLETİLMİŞ ÖZET

Evrenin gizemleri ve içindeki yerimiz, evrenin kaynağını, evrimini ve temel etkileşmelerini anlamamız için bize yol gösteriyor.-Bu arayış merakımızı artırıyor, teknolojiyi ilerletiyor ve insanlığı bilgi arayışında birleştiriyor. Big Bang veya Büyük Patlama Teorisi, evrenin yaklaşık 13.8 milyar yıl önce inanılmaz derecede sıcak ve yoğun bir noktadan nasıl başladığını açıklıyor. Bu teoriye göre evren, patlamadan sonra parçacıklar, atomlar, galaksiler ve yıldızlar yaratarak hızla genişledi. Kozmik mikrodalga arka plan radyasyonu bu teoriyi desteklemektedir. Evren halen genişlemeye devam ediyor ve gözlemler onun geçerliliğini doğruluyor.

Parçacık fiziğinin Standart Modeli (SM), Büyük Patlama sırasında ve sonrasında var olan koşulları anlamak için çok önemli bir rol oynar. Evren son derece sıcak ve yoğun bir halden hızla genişledikçe, parçacıklar ve onlara karşılık gelen karşıt parçacıklar sıklıkla yaratılıp yok edildi. SM'in öngördüğü kuvvetler, evrenin bu ilk anlarında bu parçacık etkileşimlerinden sorumluydu. Kuarklar ve leptonlar da dahil olmak üzere maddenin oluşumu, SM'de açıklanan temel kuvvetlerden etkilenmiştir. Evren soğudukça, bu parçacıklar birleşerek ilk protonları, nötronları ve elektronları oluşturmaya başladılar.

Dahası, SM'in Higgs bozonunun diğer parçacıklara kütle kazandırdığını açıklaması, evrendeki yapıların oluşumunu anlamak için çok önemlidir. Higgs mekanizması, Büyük Patlama'dan sonra parçacıkların nasıl kütle kazandığını, atomları, yıldızları, galaksileri ve bugün gözlemlediğimiz tüm kozmik yapıları oluşturmalarına izin verdiğini anlamanın merkezinde yer alır.

SM, Büyük Patlama'dan sonra evrenin ilk anlarında rol oynayan parçacıkları ve kuvvetleri anlamak için bize bir çerçeve sağlar. Parçacıkların nasıl etkileştiğine, birleştiğine ve evrimleştiğine ışık tutar ve nihayetinde bugün bildiğimiz evrenin nasıl oluştuğunu açıklamaya çalışmaktadır.

Dünya çapında önde gelen birkaç laboratuvar, SM'deki parçacıkları ve etkileşimleri test etmekte önemli rol oynamaktadır. Kapsamlı deneyleri, veri sağlamaları ve uluslararası işbirliğini teşvik etmeleri sayesinde, bu kurumlar parçacık fiziğindeki bilgimizi önemli ölçüde ileriye taşıyor. Bu saygın laboratuvarlar arasında CERN, parçacık fiziği araştırmalarında lider olarak seçkin bir konuma sahiptir ve dünyanın en büyük ve önde gelen parçacık fiziği araştırma tesisi olarak tanınmaktadır.

BHÇ İsviçre, Cenevre yakınlarındaki CERN'de bulunan güçlü bir parçacık hızlandırıcıdır. Amacı, parçacıkları ışık hızına çok yakın hıza çıkarmak ve onları çarpıştırarak, maddenin ve evrenin temel-özelliklerini açıklamaktır.

BHÇ'nin önemi, parçacık fiziğinin SM'i ile olan yakın bağlantısında yatmaktadır. BHÇ'de yüksek enerjilerde çarpıştırılarak Büyük Patlama'dan kısa bir süre sonra oluşan benzer koşullar yeniden oluşturulmaktadır. Bu çarpışmalar, SM'in tahminlerini test etmek için değerli veriler sunan çeşitli parçacıklar üretir.

Ayrıca BHÇ, SM’in ötesini keşfetmek için bir platform görevi görür. Teori başarılı olsa da tam değildir ve birçok fizik sorusunu açıklamakta zorlanmaktadır. BHÇ’deki deneyler, mevcut anlayışımızı genişletebilecek yeni parçacıkları ve etkileşimlerı araştırmaktadır.

CMS, CERN içindeki BHÇ’de bulunan önemli bir parçacık detektörüdür. Yüksek enerjili proton-proton çarpışmalarında üretilen parçacıkları araştırarak maddenin temel yapısına ve daha geniş evrene ilişkin öngörülerde bulunmaktadır.

CMS, parçacık fiziğinde büyük bir öneme sahiptir. İlk olarak, 2012'de Higgs bozonunun tarihi keşfinde çok önemli bir rol oynamıştır. Bu keşfin ötesinde, CMS, SM’in sınırlarını aşma arayışında etkilidir. Potansiyel olarak mevcut teorik çerçevemizin sınırlarının ötesine geçen yeni parçacıkların ve fenomenlerin takibinde merkezi bir rol oynamaktadır. Bu, süpersimetri gibi teorileri keşfetmeyi, potansiyel karanlık madde adaylarını aramayı ve uzayın ek boyutlarını düşünmeyi içerir.

CMS, içiçe geçmiş dedektör katmanlarından oluşmuştur. İç izleme sistemi, çarpışmalardan kaynaklanan yüklü parçacıkların yörüngelerini ve momentumlarını titizlikle izler. Elektromanyetik kalorimetre (ECAL) elektronların ve fotonların enerjilerini ölçerken, hadronik kalorimetre (HCAL) hadronların enerjisini ölçer. Bu tasarım, parçacık özelliklerinin kapsamlı bir şekilde değerlendirilmesini ölçmektedir.

Yakalanması zor olan müonlar (μ) için en dıştaki katmanda müonları algılayan ve izlerini belirleyen müon odaları bulunmaktadır. Süper iletken bir solenoid tarafından üretilen güçlü bir manyetik alanın varlığı, yüklü parçacıkların momentumlarının doğru bir şekilde ölçülmesini sağlamaktadır. Ayrıca, iyi tasarlanmış bir tetikleme sistemi, ilgili olay verilerini etkili bir şekilde seçip yakalayarak, her bir çarpışma sırasında üretilen muazzam veri hacmi nedeniyle verimli veri işlemeyi kolaylaştırmaktadır. CMS detektörü BHÇ'nın deney düzeneğinin temel taşıdır. Çok yönlü yetenekleri sayesinde, fizikçilere parçacık davranışının inceliklerini çözme, mevcut teorileri doğrulama, yeni fizik araştırmalarına başlama ve evrenin temel bileşenlerine ilişkin kavrayışımızı genişletme gücü vermektedir.

Jetler, yüksek enerjili parçacık çarpışmalarından ortaya çıkan parçacık spreyleridir. Parçacık fiziğinin önemli araştırma konularından biri olup protonların ve nötronların temel bileşenleri olan kuarkların ve gluonların özellikleriyle ilgili bilgi verirler. Yeniden yapılandırılmış jetler, ortak bir kuark veya gluondan kaynaklanan yakından hizalanmış parçacıkların gruplandırılmasını içerir. Bu süreç, fizikçilerin ilk kuark veya gluon'un enerjisini ve momentumunu anlamasına yardımcı olur. Gelişmiş algoritmalar parçacıkları kümelerken, manyetik alanlar nedeniyle yörüngesi eğrilen parçacıkları hesaba katar.

Deneysel sonuçları anlamak için jetleri simüle etmek çok önemlidir. MC simülasyonları, parçacık etkileşimlerini taklit ederek deneysel veriler ve teorik tahminler arasında karşılaştırma yapmayı sağlar. Bu simülasyonlar jet oluşumunu yeniden üreterek dedektör kalibrasyonuna yardımcı olur ve yeniden yapılandırma algoritmalarını geliştirir.

SM'in parçacık fiziğindeki önemi birkaç alanda yatmaktadır. Jetler, SM'in hassas testlerine izin vererek güçlü kuvvet hakkında bilgi sağlar. Çiftlenim sabiti gibi temel parametrelerin ölçülmesinde büyük önem taşırlar. Tahminlerden sapmalar yeni parçacıkları veya kuvvetleri gösterebileceğinden, jetler ayrıca SM'in ötesinde yeni fiziğin tanımlanmasına yardımcı olur. Ek olarak, jetler Higgs bozonunun özelliklerini incelemek ve egzotik parçacıkları aramak için merkezi öneme sahiptir. Jetlerin analizi, yeniden yapılandırılmış verilerin simülasyonlar ve teorik modellerle karşılaştırılmasını gerektirir. Araştırmacılar enerji dağılımı, şekil ve alt yapı gibi jet özelliklerini inceler. Tahminlerden sapmalar, SM'in kesinlik testlerini kolaylaştırarak yeni fizik olaylarını ortaya çıkarabilir veya bilinen teorileri doğrulayabilir.

Jetlerin CMS içinde yeniden yapılandırılması, simülasyonu ve analizi, parçacık fiziği anlayışımızı kolaylaştırmak için bir kilometre taşı görevi görür. Temel kuvvetler için yol gösterici, teorik çerçeveleri doğrulayıcı, yeni fizik alanlarını açığa çıkarmak ve atom altı dünyanın gizemlerini çözmeye katkıda bulunmak bakımından oldukça büyük öneme sahiptirler.

HGCAL, CMS deneyi çerçevesinde çok önemli bir bileşendir. HGCAL, yüksek enerjili çarpışmalarda üretilen parçacıkların enerji birikimini yakalamak ve analiz etmek üzere titizlikle tasarlanmıştır. Kuarklar ve gluonlar gibi parçacıkların davranışlarını tespit etme ve karakterize etme konusunda özellikle ustadır. Bu yetenek, enerji birikintilerinin doğru bir şekilde konumlandırılmasını ve ölçülmesini sağlayan ince segmentli yapısından dolayıdır.

HGCAL, CMS deneyinin parçacık etkileşimlerini incelemede merkezi bir rol üstlenir. HGCAL, parçacık jetlerinin yeniden yapılandırılmasını ve analizini detaylandırmayı sağlar. Jetlerin daha iyi ölçülebilmesi güçlü kuvvetin ve Higgs bozonunun özelliklerinin anlaşılmasına ve de yerleşik çerçevelerin ötesinde yeni fizik keşiflerine yardımcı olur.

Bu tez çalışmasında HGCAL'in verimliliğini araştırmak ve değerlendirmek için hafif kuark jetlerinin simülasyon verileri üretilmiştir. Jetler yeniden yapılandırılmış ve özellikle parçacık akışı (PF) Jet dağılımları incelenmiş ve bulunan sonuçlar grafiklerle sunulmuştur. MC simülasyonları yoluyla üretilen GEN jetlerden elde edilen verilerle de karşılaştırılmıştır.

Bu dağılımlar, özellikle BHÇ içinde meydana gelenler olmak üzere, yüksek enerjili çarpışmalardan kaynaklanan jetlerin kinematik özelliklerini anlamak için vazgeçilmezdir. Jetlerin enine momentumu p_T, psedorapidite dağılımı η, ve azimut açısı φ hakkında önemli bilgileri içerir.

ACKNOWLEDGEMENTS

First of all, I express profound thankfulness to Allah for blessing me with the opportunity to embark on this journey, granting me a loving family, supportive friends, and the chance to seize the richness of life's opportunities.

I extend my sincere acknowledgement to my supervisor, Prof. Dr. İsa DUMANOĞLU, for his exceptional guidance, unwavering support, and dedicated mentoring throughout my academic journey. His invaluable contributions encompass not only his assistance in navigating the intricate terrain of particle physics but also his willingness to provide guidance and motivation that extended beyond the academic realm. His mentorship has played an integral role in shaping my understanding of particle physics and has even touched my personal life, fostering growth and resilience. His presence has been a constant source of encouragement, and I am profoundly thankful for his multifaceted contributions to both my academic and personal development.

I would also like to express my deep thankfulness to Prof. Dr. Shuichi KUNORI for his priceless direction and support during the analysis phase of my research. His expert advice and insightful suggestions greatly enriched the quality of my work.

I am highly grateful to Prof. Dr. Eda EŞKUT for her valuable counsel and enriching teaching in the realm of particle physics, which enabled me to attain a deeper understanding of this intricate subject. I extend my earnest thanks to two esteemed professors, Prof. Dr. Metin ÖZDEMIR and Prof. Dr. Faruk KARADAĞ, whose expertise illuminated critical aspects of my academic journey. A sincere thanks is owed to Prof. Dr. Aysel KAYIŞ TOPAKSU for her guidance.

I express my utmost thankfulness to Assist. Prof. Dr. Yalçın GÜLER for his firm dedication and invaluable support throughout the entirety of my analysis. His commitment to teaching and assisting me through every coding step, has been truly remarkable. His patience in explaining the intricate details of the analysis process has been instrumental in enhancing my understanding. Moreover, his diligent efforts in preparing my ntuple and analysis code have significantly contributed to the readiness of my work.

I reserve a special place of gratitude for Res. Assist. Ebru USLAN, whose generous teachings and persistent advice propelled my journey, while Dr. Ali Eren ŞİMŞEK’s valuable contributions to my analysis and coding deserve sincere recognition.

The unwavering support of my parents, Mohammad Azim and Halima QARAKHANI has been a source of motivation and encouragement. I extend my heartfelt appreciation to my all cherished friends, especially Ghezala NIAZMAND and Hosna MUJADDEDI, who stood by my side with unyielding support and inspiration, even offering financial assistance whenever needed.

I am deeply grateful to my friends QAZI Sugra Altaf and Jennifer Wainana WANJUHI, Dr.Merhan KILIÇ, Dr.Zahra Khoobkar, and Dr.Maryam Akbari whose valuable assistance went beyond measure, especially in matters concerning the intricacies of psychology and understanding emotions. Their meticulous attention to detail and encouraging words not only helped me navigate through challenges but also provided solace during the demanding phases of understanding intricate feelings. Their friendship and contributions are deeply appreciated, as they have not only shaped my academic achievement but also enhanced my comprehension of the human psyche.

I want to convey my genuine appreciation to my husband, Nariman QAEYM, whose steadfast support both financially and spiritually has been a cornerstone of my progress. He has consistently encouraged me, instilling strength and resilience in me throughout every challenge. His strong belief in my abilities has been a driving force behind my accomplishments. And also my heartfelt appreciation extends to my beloved son, Burgut QAEYM, whose presence has consistently been a wellspring of inspiration and happiness.

LIST OF TABLES

LIST OF FIGURES

SYMBOLS AND ABBREVIATIONS

GUT	Grand Unified Theory
TOE	Theory of Everything
CNB	Cosmic Neutrino Background
SM	Standard Model
QFT	Quantum Field Theory
SSB	Spontaneous Symmetry Breaking
QCD	Quantum Chromodynamics
QED	Quantum Electrodynamic
SLAC	Stanford Linear Accelerator Center
Fermilab	The Fermi National Accelerator Laboratory
LHC	Large Hadron Collider
CERN	Conseil Européen pour la Recherche Nucléaire (the European Organization for Nuclear Research)
ATLAS	A Toroidal LHC Apparatus
CMS	Compact Muon Solenoid
HGCAL	High Granularity Calorimeter
HL	High-Luminosity
ECAL	Electromagnetic Calorimeter
HCAL	Hadron Calorimeter
fm	Femtometer
TeV	Tera-electron-volt
GeV	Giga-electron volt
°C	Celsius
CP	Charge-Parity
MC	Monte Carlo
PCB	Printed Circuit Board
PF	Particle Flow
GEN	Generated

1. INTRODUCTION

1.1. Theoretical Framework

Throughout the history of humanity, our constant curiosity has driven us to seek answers about how life works and what the world is made of, from ancient times to modern science. The basic materials of everything that makes up the universe are same. Even a tiny stone can take us back billions of years, of course if we manage to decipher its language. If we look to the sky at the dark night we will see a fascinating landscape with full of starts. What if we could go a little bit further? if there were no barriers between us and starts then there would be a darkness eternity for us to comprehend it. It really is? Does not the universe have an end or a beginning? The typical definition of the universe is based on infinity "Infinite Universe Theory", unlimited dimension from one end to the other. But not everyone agrees with this idea. There is only one source of information about this which are cosmic rays. As we know nothing in the universe can go faster than the light. It means light must reach us although how far it is away. In a hypothetical situation where the universe is filled with countless stars, we would think that the night sky would always be very bright with lots of light. However, this sharply contradicts the current reality of a dark, seemingly empty nighttime sky. This puzzling problem, known as the "dark night sky paradox". The origin of this paradox can be traced back to 1823 when the German astronomer Heinrich Wilhelm Olbers first introduced it. From his explanation we can have an important assumption that universe must be finite. It must have end and a beginning point. This "beginning theory" idea first appeared scientifically in 1931 in an article by a Belgian cosmologist, Georges Lemaitre. Today this theory accepted by almost all astronomers and overturned all the assumption about Universe which we call it "The Big Bang Theory".

1.1.1. The theory of Big Bang

According to this theory, around 13.7 billion years ago, a time when neither space nor time as we know them existed, all the matter and energy within the entire expanse of the universe came together, compressing into an exceedingly minute singular point characterized by infinite density and intense heat. Perhaps, like supercharged black hole. Suddenly, a huge explosion happened, it was not an explosion, but it was all space stretching everywhere all at once, means the appearance of space and time in the universe. The energy which pushing out the fabric of space cosmic inflation transformed into an energy of matter and radiation and begun to fill our universe known as "reheating". Around 13.7 billion years ago, an initial state without space and time saw the entire universe condense into an infinitely dense and intensely hot point. This marked the beginning of expansion, albeit at a slower rate, leading to reduced density and cooling.

Roughly 13.7 billion years ago, the universe underwent a condensation from a state devoid of space and time into an intensely hot, infinitely dense point. This triggered a slower expansion, resulting in cooling and reduced density. As things cooled, fundamental particles like electrons, quarks, and photons emerged, forming the basis for particles like protons, neutrons, and electrons – the building blocks of all matter. Despite these changes, the universe remained too hot for stable atoms, causing collisions that scattered light. Around 10,000 years post-explosion, the plasma emitted energetic radiation that stretched due to expansion, followed by a cooling phase where free electrons combined with nuclei, allowing light to escape and the universe to become transparent. Gravity-driven density variations later led to the formation of stars and galaxies, about 12 billion years ago, marking the "age of re-ionization." This process, combined with clearing hydrogen gas, made the universe transparent to ultraviolet light.

Everything in the universe, including ourselves, emerged from that initial point. Studying these step-by-step processes can illuminate how this remarkable journey unfolded.

Radiation period (dominance of radiation)

- Superforce stage: between zero and approximately 10^{-43} second after the Big Bang, temperature was infinitely high, and there was no matter. In that era, the universe consisted solely of energy and the four fundamental forces of nature: Gravity, Strong Nuclear, Weak, and Electromagnetic forces. These four forces were a single fundamental force which is called Superforce and this stage is also called *Planck Epoch*. As well as, this early stage is described by Unified Field Theory or Theory of Everything (TOE).
- Grand unified stage: at the 10^{-43} of a second, when the temperature cooled to 10^{32} Celsius (°C), *Gravity* split away from Superforce and began operate the universe while remaining Strong Nuclear, Weak and Electromagnetic forces stabilize into the Electronuclear or Grand Unified Force which is explained by Grand Unified Theory (GUT).
- Electroweak stage: at the 10^{-36} of a second of Big Bang, temperature decreased to $\approx 10^{28}$ °C or 10^{16} giga electron volt (GeV) and causes to breaking away of Strong Nuclear from Electronuclear force. As a result, Weak and Electromagnetic forces acted as a single Electroweak force.
- Cosmic inflation stage: at 10^{-33} of a second the universe experienced rapid expansion at a velocity exceeding that of light and grew exponentially by a factor of the 10^{26} between fraction of time from 10^{-33} to 10^{-32} of a second. Temperature also dropped down from about 10^{27} °C down to 10^{22} °C. Some scientists propose that this inflation could be enduring and might have given rise to a *Multiverse* comprising distinct universes referred to as *Parallel Universes*.
- Plasma stage: approximately 10^{-32} second after the Big Bang, inflation concluded, and the universe continued to cool. During this phase, the essential building blocks of the universe, including quarks, electrons, antiquarks, leptons, and neutrinos, came together in a hot, ionized gas mixture known as *Quark-Gluon Plasma*. All particle was in thermal equilibrium. The hypothesized components of cold dark matter (*axion*) may also have formed at this time.

- Universe under four governors' stage: at 10^{-12} of a second, when the temperature is ≈ 10^{15} °C enough cool to split up Weak and Electromagnetic forces from each other and now the four fundamental forces started to working as separate forces. Matter particles have the ability to engage with the Higgs Field, thereby acquiring mass.
- Baryogenesis stage*:* Around 10^{-11} second after the explosion, a hypothesis suggests that matter might have outnumbered antimatter due to an imbalance between baryons and antibaryons. This contradicts the assumption of equal matter and antimatter production during the Big Bang. This hints at differing physics for these particles or their absence. Several hypotheses attempt to explain this matter-antimatter disparity, but a consensus theory remains elusive.
- Hadron stage*:* Around 10^{-6} second after the start, when the universe had stretched to billions of kilometers in diameter, it became less dense and cooled to about 10^{10} °C or 1 mega electron volt (MeV). At this point, the original quark-gluon plasma transitioned into hadrons, including baryons and mesons. This transformation was driven by the strong nuclear force.
- Lepton stage*:* In the first second after the Big Bang, as the universe cooled to around ≈ 10^{9} °C, hadrons and anti-hadrons annihilated, leaving behind leptons. This led to leptons becoming the dominant mass in the universe. Under the influence of gravity, as the universe expanded, neutrinos separated from matter, forming a cosmic neutrino background. Due to the universe's expansion, particle interactions slowed down and particles moved out of thermal equilibrium. This gave rise to the *Cosmic Neutrino Background* (CNB), a particle radiation composed of neutrinos, with a temperature of about 1.95 °C.
- Photon stage*:* 10 seconds later, most of the leptons and antileptons annihilated each other. As electrons and positrons annihilated, the universe dominated by photons of radiation as shown in Figure 1.1.

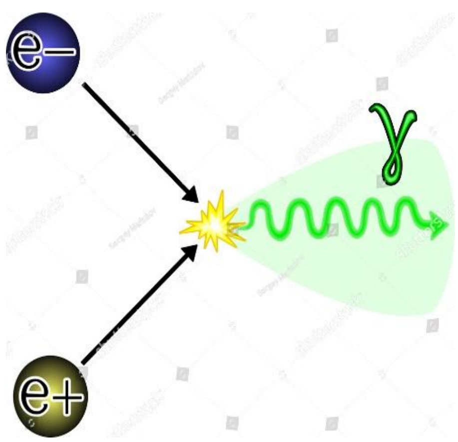

Figure 1.1. Leptons and antileptons annihilated, paving way for a photon-dominated universe. (https://www.shutterstock.com/tr/image-vector/electron-positron-annihilation-772129372 [last access date: 20.06.2023])

Particles of matter coupled with light and radiation, dark matter particles begun to form nonlinear structures as dark matter halos. But a small number of unpaired electrons were left over. As a result, positrons disappeared. But the exact reason that why did it happen still mystery. Because the charged electrons and protons block the emission light, the universe became a super-hot glowing fog.

- Nucleosynthesis stage: well, 3 minutes passed, universe were enough cold to combine proton and neutron to form very first atomic nuclei the Deuterium (^2_1H), and temperatures and densities sufficiently high for fusion reactions to take place hereby the nuclear fusion[1] begun at a significant rate. In this process most of the Helium as isotopes Helium-3 (^3_2He), Helium-4 (^4_2He), and heavy Hydrogen isotopes Deuterium (^2_1H) and Tritium (^3_1H or T) were formed. Finally, Lithium isotope Lithium-7 (^7_3Li) and Beryllium isotope Beryllium-7 (^7_4Be) began form between 100 and 300 seconds. But radioactive isotopes which are ^7_4Be and ^3_1H because of being unstable, they decayed into ^7_3Li and ^4_2He respectively. We can see this process in Figure 1.2.

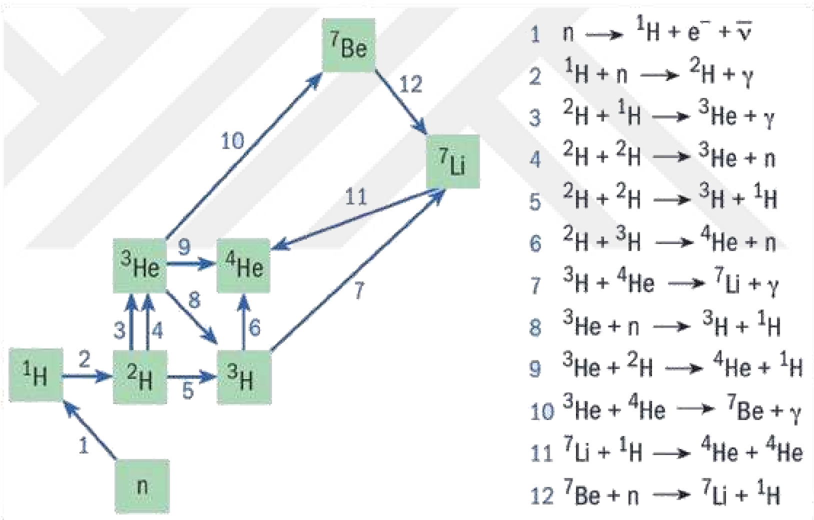

Figure 1.2. The process of Big Bang nucleosynthesis (https://universe-review.ca/I14-03-BBN.jpg [last access date:14.10.2023]

Elements heavier than beryllium could not form because of the very short time (about 20 minutes). Elements created during this period existed in a plasma state and only transitioned to neutral atoms much later as they cooled down.

- Last Stage of Radiation Stage: After about 20 minutes, as the universe expanded and its thermal energy dropped below 0.03 MeV, high-energy collisions among nucleons ceased. This led to the predominance of simpler reactions, resulting in the universe being composed of

[1] Nuclear fusion is the process of atomic nuclei merging, resulting in the formation of new nuclei and the release of particles such as neutrons or protons.

approximately75% ${}^{1}_{1}H$, 25% ${}^{4}_{2}He$, around 0.01% ${}^{2}_{1}H$ and ${}^{3}_{2}He$, with fewer heavier elements. These observed abundances align with predictions, providing strong support for the Big Bang theory. Meanwhile, free electrons began scattering light. The universe contained a dense, hot plasma of nuclei, electrons, and photons.

Matter period (dominance of matter)

The Period of Matter marks a significant phase in the universe's evolution, characterized by the prevalence of matter. It encompasses three key epochs: Atomic, Galactic, and Stellar, spanning billions of years, including the present.

- Equivalence of Matter and Radiation: Approximately 47,000 years post the Big Bang, during a period of rapid universal expansion, matter and radiation coexisted in equal proportions.
- Matter Domination: Gradually, matter particles dominated over radiation. This period played a important role in shaping the universe's structure, fostering galaxy and cosmic structure formation. This era represents a significant shift in the universe's dynamics.
- Cosmic Dark Age*:* Roughly 370,000 years later, the thermal energy dropped to ≈3000°C or 0.25 eV. This facilitated electron bonding to nuclei, forming electrically neutral atoms, predominantly hydrogen and helium.
- Reionization Stage*:* Around 100 million years later, ordinary matter particles collapsed into structures formed by dark matter. This resulted in the emergence of smaller structures like stars and larger ones like quasars, emitting ultraviolet light that ionized the remaining neutral gas.
- Recombination Stage*:* Between 200-300 million years post-Big Bang, hydrogen atoms combined with helium, forming atomic clouds. Within these clouds, gravity caused atoms to clump together, forming the seeds of galaxies. This phase marked the birth of the first stars.
- Galaxy Stage*:* After roughly 1 billion years, normal galaxies developed. Reionization concluded, with intergalactic space no longer showing absorption lines from neutral hydrogen. Photon scattering by free electrons decreased as the universe expanded, and galaxies formed while intergalactic space turned transparent. Galaxy evolution continued, leading to the formation of more modern-looking galaxies, some of which merged to create larger structures.

Scientists have learned a lot about how the universe began and works, but there are still many things we don't know. To figure out how the universe started and the processes that made it the way it is, scientists need to keep studying and doing experiments.

Progress necessitates a systematic approach, grounded in a thorough understanding of fundamental particles and their interactions. This foundation will enable comprehensive insights into the universe's mechanisms.

As we continue our exploratory journey, each discovery becomes a valuable puzzle piece, contributing to the unraveling of cosmic secrets. Through cumulative efforts in understanding particles, their properties, and interactions, we aim to answer the universe's most profound questions.

1.2. Fundamental interaction

The fundamental interactions, often called fundamental forces, are the basic ways things in nature interact without breaking down further. Four main interactions control how particles and matter behave:

1. Gravity: Pulls objects with mass together, like planets and stars in space.
2. Electromagnetism: Deals with electric charges, magnets, and even light.
3. Weak Interaction: Handles changes in tiny particles, like those in atoms.
4. Strong Interaction: Holds protons and neutrons tight inside atomic nuclei.

These interactions shape everything around us, explaining actions from planet motion to atom behavior. They're vital for understanding nature's laws.

1.2.1. Gravity

Gravity causes objects with mass to be drawn toward each other. Among the four forces, it's the weakest yet the most influential on a grand scale. While it's hardly noticeable at the tiniest levels of particles, it takes center stage when dealing with planets, stars, and galaxies. Think of it as the cosmic choreographer, orchestrating the movements of celestial bodies and even guiding the paths of light rays.

Gravity's reach is limitless, but its strength wanes as things move apart. Early in the universe's history, gravity's pull caused scattered matter to unite, giving birth to stars and galaxies. An interesting quirk is how gravity transforms the fabric of space-time itself. This phenomenon is elucidated by Albert Einstein's theory of relativity, describing gravity not as a traditional force, but as the curvature of the very fabric of reality.

Black holes exemplify the profound influence of gravity's curvature. These cosmic sinkholes are so gravitationally intense that not even light can escape their clutches beyond a certain point called the event horizon.

For most day-to-day situations, Isaac Newton's law of universal gravitation works just fine. The theory asserts that the force between two attracted objects is directly related to their mass and inversely related to the square of the distance that separates them. Eq (1.1)

$$F = G\frac{m_1 m_2}{r^2} \tag{1.1}$$

This simple formula allows us to predict how objects on Earth and in the cosmos interact due to gravity.

Yet, the story of gravity doesn't end there. Scientists delve into its origins during the universe's infancy. They're searching for ways to reconcile gravity with quantum mechanics, aiming to merge these fundamental principles into a comprehensive theory of everything. This would provide a unified understanding of all the forces shaping our universe, from the tiniest particles to the grandest galaxies.

1.2.2. Electromagnetism

The electromagnetic force is what holds atoms and molecules together. On a bigger scale, the electromagnetic force is responsible for many everyday phenomena, from atoms sticking together to forming molecules. It's been refined over time with new physics like quantum mechanics and relativity. It even inspired Einstein's theory of special relativity. Quantum Electrodynamics (QED) examines it in the quantum world, showing that electromagnetic fields are made of particles called photons.

But there's still a lot we don't know, like magnetic monopoles and how certain creatures sense electric and magnetic fields.

1.2.3. Weak interaction

The weak interaction handles radioactive decays. It's got long lifetimes and tiny cross sections, meaning it's not very strong. All fermions, the building blocks of matter, feel it, but usually, strong and electromagnetic forces take the spotlight. There's a special group of particles called neutrinos that only feel the weak interaction. That's why studying them is tricky; they only experience this one force, unlike the others.

This process includes the exchange of particles known as W and Z vector bosons. They're hefty, around 80 GeV, and because of this, they can only act over incredibly short distances, about 0.1% of a proton's diameter. The weak interaction is responsible for changing one flavor of quark into another, which has a big impact on how the universe is structured.

The sun relies on the weak interaction to burn because it transforms protons into neutrons, allowing deuterium to form and fusion to occur. It's also vital for building heavy atomic nuclei. The weak interaction is the key player in processes where quarks change flavors, which we can see in various nuclear decays.

Interestingly, the weak interaction is unique because it's the only one that can change one type of fermion into another. It's like a down quark becoming an up quark by emitting a W^- boson. Other forces don't do this, they don't change the identity of the particles they interact with. This

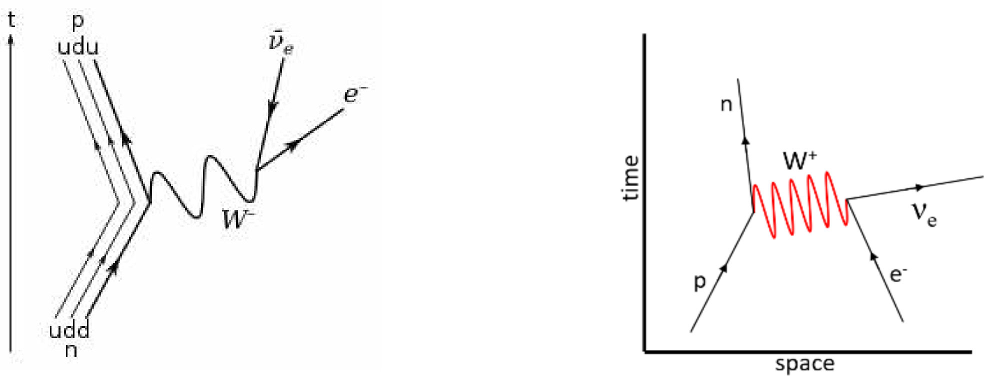

Figure 1.3. β-decay processes by weak interaction
(https://en.wikiversity.org/wiki/Beta_decay [last access date: 20.06.2023])

interaction affects both quarks and leptons, the two main categories of particles. Two examples of weak interaction is shown in Figure 1.3. The illustration on the left depicts a neutron in isolation undergoing decay through the emission of a W^- particle, resulting in the creation of an electron and an antineutrino $n^0 \longrightarrow p^+ + e^- + \bar{\nu}_e{}^0$. Meanwhile, the diagram on the right portrays a scenario in which a proton, through weak interaction, captures an electron to transform into a neutron, as illustrated by this Feynman diagram $\mathrm{p}^+ + \mathrm{e}^- \longrightarrow \mathrm{n}^0 + \nu_\mathrm{e}{}^0$.

1.2.4. Strong Interaction

Imagine a force that defies strong repulsion to keep a nucleus whole. Unlike electromagnetism, it has a limited reach and behaves uniquely.

Yukawa's idea explains this force as particles like pions being exchanged, similar to a game of ping-pong. The uncertainty principle restricts their range. This force stands as the most powerful among the fundamental forces. Protons and neutrons contain quarks within them, bound together by the "color force." The strong force results from this color force. The glue that holds quarks is carried by *gluons*. Their presence in protons and neutrons prevents using their mass to predict the force's range.

When something emerges from a proton or neutron, it takes the form of a quark-antiquark pair. The lightest meson, the pion, reflects the maximum range of this force. It's like the pion carries

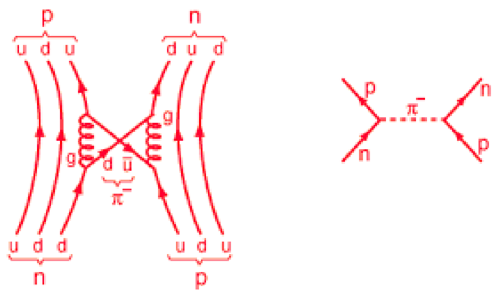

Figure 1.4. Quarks combining as up-antiup pairs can lead to π^-particle formation, creating a bridge between nucleons. (http://hyperphysics.phy-astr.gsu.edu/hbase/Forces/funfor.html [last access date: 20.06.2023])

the message of this potent yet short-range force. As depicted in the Figure 1.4.

1.3. The Particle Physics Standard Model

The of Particle Physics SM stands as our prevailing framework to elucidate the fundamental building blocks of the natural world and interaction between them. These particles are deemed "elementary" or "fundamental," signifying their indivisibility into smaller components.

The SM posits three generations of particles, each mirroring the others. Each generation comprises two kinds of quarks, two kinds of leptons, and their corresponding antiparticles. As shown in Figure 1.5. The first generation forms everyday matter like protons and electrons. The second and

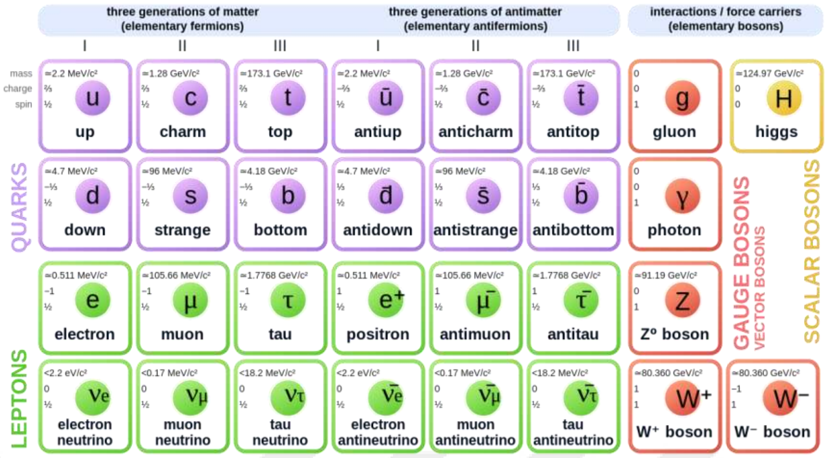

Figure 1.5. Fundamental constituents of the SM (https://sciencex.com/news/2021-04-proof-physics-muon-magnetic-moment.html [last access date: 20.06.2023])

third generations, resembling heavier versions, observable in high-energy collisions, like those observed in particle colliders and cosmic ray events. While the SM triumphantly explains and predicts various particle physics phenomena, it remains incomplete, leaving questions unanswered - dark matter's nature and the unification of fundamental forces. The quest for new particles and interactions persists, promising deeper insights into the universe's essence.

Each particle holds unique attributes like mass, electric charge, and spin, a persistent angular momentum even at rest. The spin quantum number, denoted as s, assumes fixed values for particle types. Half-integer spin defines *fermions*, like electrons, while integer spin characterizes *bosons*. The SM categorizes particles into three groups: leptons, quarks, and gauge bosons. Quarks and leptons exhibit half-integer spin (1/2), while gauge bosons have a spin of 1. The spin−0 Higgs boson is proposed to elucidate mass origin.

Leptons include the electron and electron neutrino are affected by electromagnetic and weak interactions. Hadrons, like neutrons and protons, consist of quarks held together by the strong interaction. Gauge bosons are responsible for mediating the strong, weak, and electromagnetic forces. Electromagnetic interactions involve photons as force carriers. Weak interactions involve massive W^+ and W^- bosons, and strong interactions entail massless gluons. Notably, a consistent quantum theory of gravity has not yet been developed.

The SM clarifies three fundamental forces (excluding gravity) and categorizes particles. Developed over decades, its present form solidified during the mid-1970s, with experimental confirmation of quarks. Subsequent discoveries like the top quark, tau neutrino, and Higgs boson reinforced its validity.

The SM is a prevailing framework illuminating particle physics, yet leaves questions unanswered, fueling ongoing exploration into the universe's intricacies. It is encompassing three fundamental forces: electromagnetism, weak interaction, and strong interaction. Represented by :

$$GSM = SU(3)_C \otimes SU(2)_L \otimes U(1)_{Y_w}$$

$U(n)$ represents unitary and $SU(n)$ special unitary groups with order n ∈ N. Within this framework, three of the fundamental forces are encompassed. It classifies particles into families and accounts for their interactions through gauge bosons.

However, the SM does not encompass the fourth fundamental force, gravity, and its theorized messenger, the graviton is a massless spin-2 boson which remains elusive. This absence prompts an ongoing quest for a unified theory encompassing gravity within the particle framework.

For clarity, Table 1.1 presents a comparison of the four fundamental forces.

Table 1.1. Comparing Fundamental Interactions (https://selfstudypoint.in/fundamental-forces-nature/ [last access date:08.24.2023])

Interaction	Carrier	Interacts with	Rel. Strength	Range
Strong	gluon (g)	color charge C	1	10^{-15}m
Electromagnetic	photon (γ)	electric charge Q	10^{-2}	∞
Weak	$W^{\pm}$, Z^0	weak isospin T3	10^{-13}	10^{-18} m
Gravitational	graviton (G)	mass m	10^{-39}	∞

1.3.1. Leptons

Leptons, a group of fundamental particles with a spin of 1/2 are fermions that do not experience strong interactions. Comprising six distinct types occurring in pairs known as generations, they are denoted as doublets:

$$\begin{bmatrix} \nu_e \\ e^- \end{bmatrix} \begin{bmatrix} \nu_\mu \\ \mu^- \end{bmatrix} \begin{bmatrix} \nu_\tau \\ \tau^- \end{bmatrix}$$

In each generation, there is a charged lepton possessing an electric charge of Q = -e, accompanied by a neutral lepton, often referred to as a neutrino. These three charged leptons consist of the well-known electron e^-, along with two heavier particles called the muon μ^- and the tauon τ^-. Corresponding neutrinos of the types ν_e – electron neutrino, ν_μ – mu neutrino and ν_τ – tau neutrino have masses at the minimum threshold. Six antiparticles (antileptons) complement these leptons.

$$\begin{bmatrix} \bar{\nu}_e \\ e^+ \end{bmatrix} \begin{bmatrix} \bar{\nu}_\mu \\ \mu^+ \end{bmatrix} \begin{bmatrix} \bar{\nu}_\tau \\ \tau^+ \end{bmatrix}$$

Excluding gravity, charged leptons engage with electromagnetic and weak forces, while neutrinos solely exhibit weak interactions, rendering their detection challenging due to their minute masses. Electrons and neutrinos remain stable, soon explained. Muons, on the other hand, undergo decay due to weak interactions, and they have a relatively short lifetime of 2.2×10^{-6} seconds.

$$\mu^{+} \rightarrow e^{+} + \nu_e + \bar{\nu}_{\mu} \qquad\qquad \mu^{-} \rightarrow e^{-} + \bar{\nu}_e + \nu_{\mu}$$

This decay exemplifies the core principle of conserving lepton numbers.

Lepton Number Conservation

Each lepton generation is tied to a conserved quantum property known as lepton number. The lepton number, which is also called the number of electrons, is defined for any state as follows:

$$L_e \equiv N(e^{-}) - N(e^{+}) + N(\nu_e) - N(\bar{\nu}_e)$$

where *N(e^-)* represents the count of electrons and *N(e^+)* is the count of positrons, and so forth.
In single-particle states, L_e takes the value of 1 for e^- and ν_e, -1 for e^+ and $\bar{\nu}_e$, and remains at 0 for all other particles. Similarly, we define the muon number and tauon number as follows:

$$L_{\mu} \equiv N(\mu^{-}) - N(\mu^{+}) + N(\nu_{\mu}) - N(\bar{\nu}_{\mu})$$

and

$$L_{\tau} \equiv N(\tau^{-}) - N(\tau^{+}) + N(\nu_{\tau}) - N(\bar{\nu}_{\tau})$$

These numbers remain zero for particles apart from leptons, including photons, protons, or neutrons. In states with multiple particles, individual lepton numbers sum up. As an example, the final state in the β-decay of a neutron:

$$n^0 \longrightarrow p^{+} + e^{-} + \bar{\nu}_e{}^{0}$$

$$L_e \equiv L_e(p) + L_e(e^{-}) + L_e(\bar{\nu}_e) = 0 + 1 + (-1) = 0$$

Every lepton number retains its value throughout reactions in the electromagnetic interactions, this simplification occurs preserving $N(e^-) - N(e^+)$, $N(\mu^-) - N(\mu^+)$, and $N(\tau^-) - N(\tau^+)$, excluding neutrinos. Consequently, charged leptons emerge or disappear exclusively in pairs of particles – antiparticle. For instance, an electromagnetic reaction annihilates an electron pair while creating a muon pair (Figure 1.6).

$$e^{+} + e^{-} \rightarrow \mu^{+} + \mu^{-}$$

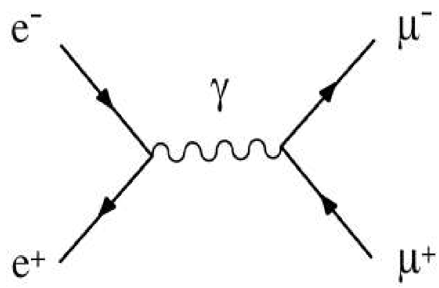

Figure 1.6. Contribution from single-photon exchange to the reaction.
(https://tr.overleaf.com/learn/latex/Feynman_diagrams [last access date: 20.07.2023])

Neutrinos

Neutrinos, captivating and elusive entities, hold a prominent role within the SM. Classified as fundamental entity, they form a subset of leptons alongside electrons and muons. Notably, neutrinos lack electric charge, rendering their detection intricate as they solely interact via the weak nuclear force and gravity. This characteristic enables neutrinos to effortlessly traverse matter, including Earth, with minimal interaction, rendering direct observation a formidable challenge.

In accordance with the SM, three distinct flavors of neutrinos exist: electron neutrinos, muon neutrinos, and tau neutrinos, each associated with a specific lepton. Natural processes like nuclear reactions occurring in the Sun and the interactions of cosmic rays with Earth's atmosphere perpetually generate neutrinos.

A groundbreaking revelation pertains to neutrino oscillations, indicating their capability to change flavor during travel through space. This revelation implies neutrinos possess mass, a factor not initially integrated into the original SM. Unraveling the properties and behavior of neutrinos remains a fervently studied endeavor. Comprehending neutrinos holds paramount importance, as it results in a deeper understanding of the fundamental properties of matter and the broader universe.

1.3.2. Quarks and Hadrons

Over 200 particles that experience strong interactions have been documented, each possessing electric charges that are either zero or integers: 0, ±1, or ±2, measured in e unit. We use the term hadrons to describe these entities and represent composite structures formed by fundamental spin -1/2 constituents known as quarks. Quarks exhibit electric charges of either +2/3 or -1/3, while their counterparts, antiquarks, carry charges of −2/3 or +1/3. Direct observation of individual quarks has not occurred in isolation as independent entities, but there is strong and convincing evidence to support their existence. This evidence comes from three main domains: the study of hadron properties, interactions involving leptons, and the analysis of particle sprays known as jets.

1. *Hadron Spectroscopy*: Hadron spectroscopy is all about studying the basic characteristics of particles called hadrons. These properties include their mass, how long they exist before decaying, and their behavior when they break apart. By looking at these features, scientists were able to find evidence for the existence of quarks, which are tiny particles that make up hadrons. The fact that the behavior of hadrons matches what the quark model predicts gives strong support to the idea that quarks are real building blocks of matter.
2. *Lepton Scattering:* Back in 1969, the presence of quarks with point-like properties within protons and neutrons came to light through the phenomenon of leptons with high-energy (including electrons, muons, and neutrinos) being deflected at significant angles when interacting with these particles. This discovery mirrored the way Rutherford and colleagues unveiled the nucleus's existence in 1911 by investigating the substantial angle deviations of high-energy charged particles as they engaged with atoms.
3. *Jets in high energy collision:* When collisions occur with high energy, the quarks housed within hadrons or the recently formed pairs of quark-antiquark can become energetically separated. Subsequently, these quarks transition into clusters of hadrons, known as jets, through relatively mild interactions. These jets bear a strong resemblance to the attributes of the quarks from which they originated. The initial sighting of jets took place in 1979 at the DESY laboratory during electron-positron collisions. After this discovery, jets have been witnessed in a range of reactions, furnishing valuable insights into the behavior of quarks within processes involving substantial energy levels.

The Six Recognized Quarks

Presently, we are acquainted with six distinct categories, referred to as flavors, of spin -1/2 quarks. Much like leptons, they manifest in pairs termed generations, designated as follows:

$$\begin{bmatrix} u \\ d \end{bmatrix}, \begin{bmatrix} c \\ s \end{bmatrix}, \begin{bmatrix} t \\ b \end{bmatrix}$$

Within each generation, a quark carrying a charge of +2/3 such as u, c, or t is coupled with a quark holding a charge of -1/3 which can be d, s, or b, both values measured in units of e. The quarks in question are known as the down (d), up (u), strange (s), charmed (c), bottom or beauty (b), and top (t) quarks. The corresponding antimatter counterparts are designated as:

$$\begin{bmatrix} \bar{d} \\ \bar{u} \end{bmatrix}, \begin{bmatrix} \bar{s} \\ \bar{c} \end{bmatrix}, \begin{bmatrix} \bar{b} \\ \bar{t} \end{bmatrix}$$

These antiquarks bear charges is 1/3 for $\bar{d}$, $\bar{s}$, $\bar{b}$ and -2/3 for $\bar{u}$, $\bar{c}$, $\bar{t}$.

Table 1.2 provides approximate values for the masses of quarks. Apart from the top quark, indirectly, these masses are determined by analyzing the observed masses of the composite bound states they form in conjunction with models describing the binding of quarks.

Table 1.2. Properties of Quarks (Riccardo, D.S., and Graziano,B., 2014. Measurement of top quark pairs production cross-section in the semi-leptonic channel with the ATLAS experiment. PhD Thesis. p-4.)

Name	Symbol	Mass	Charge (Q)	Lifetime (sec)
Down	d	$\approx 4.8\ \mathrm{MeV/c^2}$	$-{}^{1}/_{3}$	10^{-23}
Up	u	$\approx 2.4\ \mathrm{MeV/c^2}$	${}^{2}/_{3}$	5×10^{-25}
Strange	s	$\approx 104\ \mathrm{MeV/c^2}$	$-{}^{1}/_{3}$	$1.24\ x\ 10^{-8}$
Charmed	c	$\approx 1.27\ \mathrm{GeV/c^2}$	${}^{2}/_{3}$	$1.1\ x\ 10^{-12}$
Bottom	b	$\approx 4.2\ \mathrm{GeV/c^2}$	$-{}^{1}/_{3}$	$1.3\ x\ 10^{-12}$
top	t	$\approx 171.2\ \mathrm{GeV/c^2}$	${}^{2}/_{3}$	$5.7\ x\ 10^{-25}$

The durability of quarks confined within hadrons mirrors the resilience observed in protons and neutrons when they are encapsulated within atomic nuclei. The interaction energies between them influences this stability. Nonetheless, in the cases of the s, c, and b quarks, these impacts are relatively inconsequential, allowing approximate lifetimes to be assigned. The s quark boasts an approximate lifetime ranging from 10^{-8} to 10^{-10} seconds, while both the c and b quarks exhibit lifetimes within the range of 10^{-12} to 10^{-13} seconds. Contrarily, due to its notably greater mass, the top quark features a lifetime on the order of 10^{-25} seconds. This short lifetime results in top quarks decaying too swiftly upon creation to manifest as observable hadrons.
Unlike the other quarks, we learn about the top quark by studying what it turns into when it decays.

Quark Quantities

Within the context of strong and electromagnetic interactions, quarks are solely capable of emerging or vanishing as pairs of particles and their corresponding antiparticles. This principle indicates that, for instance, in electromagnetic processes represented by Feynman diagrams, the reaction $e^{+} + e^{-} \rightarrow c + \bar{c}$ is permissible, while the reaction $e^{+} + e^{-} \rightarrow c + \bar{u}$, which results in a $c\bar{u}$ air, is prohibited. More generally, this principle enforces the conservation of each of the six quark quantities.

$$N_f \equiv N(f) - N(\bar{f}) \qquad (f = \mathrm{u, d, s, c, b, t})$$

In weak interactions, a broader range of possibilities is allowed, with only the total quark quantity being conserved.

$$N_q \equiv N(q) - N(\bar{q})$$

For instance, a primary decay mode of the charmed quark involves $c \rightarrow s + u + \bar{d}$, in this process, an s quark replaces a c quark, simultaneously, u quark produces along $\bar{d}$ antiquark together. This process evidently contravenes the conservation of the quark quantities N_c, N_s, N_u and N_d. However, the overall quark quantity N_q remains unaltered. Practically, it is appropriate to talk about quark number N_q in terms of the baryon number, denoted as:

$$B \equiv \frac{N_q}{3} = \frac{[N(q) - N(\bar{q})]}{3}$$

Like the way lepton numbers and electric, the conservation of baryon number is a fundamental principle maintained in all interactions.

Baryons and Mesons

The intricate characteristics of atoms and nuclei find their elucidation through the comprehension of their foundational constituents: protons, neutrons, and electrons. While certain intricacies defy precise calculation, direct investigation of these elemental constituents becomes attainable through laboratory experiments, free from the complexity of atoms or nuclei. Although atomic and nuclear physics no longer occupy a central role in fundamental study, they persist as pivotal components in shaping our comprehension of the world.

When delving into the realm of hadrons, akin to protons and neutrons, their traits find explanation through the elemental quark components. Nevertheless, isolating quarks for individual study proves unfeasible; the exploration of quarks remains tethered to experimental measurements conducted on hadrons. Hadrons manifest in three distinct forms: baryons, constituted by three quarks (3q); antibaryons which are the antiparticles of baryons, composed of three antiquarks ($3\bar{q}$); and mesons (possessing integer spin), constructed with one quark and one antiquark ($q\bar{q}$). Baryons have a baryon number of 1, while antibaryons have a baryon number of -1, and mesons have a baryon number of 0.

Baryons and antibaryons cancel each other in reactions, while still preserving the total number of baryons. This interaction leads to the creation of mesons, and occasionally even photons or paired lepton-antilepton combinations. Noteworthy examples include the proton and neutron, the lightest baryons, both composed of three quarks each. A glimpse into the world of baryons and mesons, accompanied by their distinctive quark compositions, is provided in Table 1.3.

Table 1.3. Examples of Baryons and Mesons, Along with Their Quark Compositions (https://nuclear-power.com/wp-content/uploads/2016/11/Hadrons-Baryons-Mesons-min.png [last access date: 24.08.2023])

Particle	Composition	Mass (MeV/c^2)	Lifetime (sec)
π^+	$u\bar{d}$	140	2.6×10^{-8}
π^0	$u\bar{u}, d\bar{d}$	135	8.4×10^{-17}
K^+	$u\bar{s}$	494	1.2×10^{-8}
K^{*+}	$u\bar{s}$	892	1.3×10^{-23}
D^-	$d\bar{c}$	1869	1.1×10^{-12}
B^-	$b\bar{u}$	5278	1.6×10^{-12}
p	uud	938	Stable
n	udd	940	887
Λ	uds	1116	2.6×10^{-10}
Λ^{++}	uuu	1232	0.6×10^{-23}
Ω^-	sss	1672	0.8×10^{-10}
Λ_c^+	uds	2285	2.1×10^{-13}

Color

While the quark model calculation effectively accounts for the hadron spectrum, it leaves us with intriguing questions. One pertains to the limited observance of only 3q, $3\bar{q}$, and $q\bar{q}$ states. Another emerges from an assumption necessitated by the observed hadron spectrum alignment. The assumption is bases on pairs of two quarks with same flavor (uu, dd, ss, and so forth). Given their shared spatial state, it's inferred that their spins are parallel. However, a paradox arises from the Pauli exclusion principle, a quantum physics theorem stating that fermions that are identical cannot exist in the same quantum state.

Consider the case of Ω^- = sss,, where three identical s-quarks appear to occupy both the same space and spin states. However, the Pauli exclusion principle suggests that this cannot be the case. Resolving this quandary demands the introduction of a novel quark degree of freedom, exclusive to quarks and not leptons, intriguingly termed colors. Key characteristics of colors encompass:

1. Existence of Colors: Any quark of u, d, s, c, b, and t can manifest in three distinct colors: red, green, and blue.
2. Conserved Color Charges: Conservation is a rule in the world of tiny particles. The total "color charge" in a group of particles must always add up to zero, like positive and negative charges cancel each other. This rule makes sure that quarks, which are the building blocks of these particles, are always stuck together in groups called hadrons and never float around by themselves.

Jets and Gluons

In the field of high-energy particle physics, jets refer to focused sprays of particles that come about during particle collisions. These jets play a vital role in helping us comprehend the underlying behaviors of quarks and gluons within Quantum Chromodynamics (QCD), the theory that delves into the nature of the strong force. An intriguing observation in many high-energy particle collisions is the emergence of what we call hadron jets, as demonstrated in Figure 1.7. The event was captured during the collision of e^+ and e^- in a setup referred to as the drift chamber. This interaction takes place at the central region of the environment, where the two particle beams collide directly. One beam travel on the plane of the paper, while the other beam extends beyond it. Charged particle paths are depicted as solid lines, whereas the trajectories of neutral particles are shown as dashed lines. Detection of the neutral particles occurs through alternate methods outside the immediate vicinity.

These jets are formed in various reactions and provide us with a glimpse into what might be the closest approximation to the tracks left behind by quarks and gluons. To better understand how these jets come about, let's look at high-energy collisions involving the annihilation of electron and positron pairs:

$$e^+ + e^- \rightarrow \text{hadrons}$$

Electron-positron annihilation is a phenomenon where e^- and e^+ come together and mutually annihilate, leading to the production of high-energy photons (γ). However, at higher energies, additional processes can occur, such as the creation of quark-antiquark pairs. Let's delve into the process in more detail:

a. Electron-Positron Annihilation (γγ Production): When electron-positron annihilation occurs at lower energy levels, the predominant result is the creation of two gamma-ray photons (γγ), as exemplified by the following reaction:

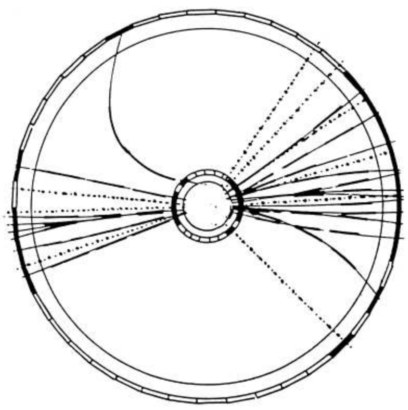

Figure 1.7. Hadron jets captured during the collision of e^+ and e^- in the drift chamber. (https://www.quantumdiaries.org/ [last access date : 21.07.2023])

$$e^{-} + e^{+} \rightarrow \gamma + \gamma$$

The gamma-ray photons generated in this process carry off the entire energy of the electron-positron system. Their energy levels correspond to the rest mass energy of both the electron and positron, each of which is roughly 511 KeV.

b. Quark-Antiquark Pair Production: At higher energies (typically in the GeV or TeV range), electron-positron annihilation can produce additional particles due to the energy being available to create more massive particles. Specifically, the high-energy photons generated during the annihilation can convert their energy into the mass of a $q\bar{q}$ pair. The reaction can be represented as follows:

$$e^{-} + e^{+} \rightarrow \gamma \rightarrow q + \bar{q}$$

Within this process, the photon undergoes an event termed "splitting" or "fluctuation," which leads to its transformation into a quark and an antiquark. These freshly formed quark and antiquark entities subsequently possess the capability to combine and shape diverse hadrons, including mesons or baryons, under the influence of the robust nuclear force.

c. Hadronization: Once the pair of quark-antiquark is produced, the quarks experience the strong force and start to interact with each other. Coming together, they create color-neutral composite entities known as hadrons. The process of quarks combining to form hadrons is known as "hadronization" or "hadron formation." The process of electron-positron annihilation and the subsequent generation of quark-antiquark pairs has been extensively investigated through high-energy particle physics experiments. These studies have yielded crucial insights into the underlying essence of quarks, the potent nuclear force, and the distinct attributes of hadrons.

Quark Jets

Within the energy span of 15–40 GeV at the center-of-mass, the sequence of electron-positron annihilation resulting in hadrons follows a two-step progression. Initially, a primary electromagnetic event occurs where the collision of e^{+} and e^{-} leads to the generation of a quark-antiquark pair. Afterward, this is followed by a strong interaction process known as fragmentation. Fragmentation effectively transforms the high-energy $q\bar{q}$ pair into two distinct jets of hadrons. These jets disperse in opposite directions within the center-of-mass frame, preserving momentum conservation. A visual representation of this phenomenon is presented in Figure 1.8, derived from collision of an electron-positron experiment.

The intricacies of the fragmentation process yield diverse particle counts and types within the jet, coupled with their respective momenta distinct from event to event. Despite this complexity, the trajectory of a jet, characterized by the combined momentum of all particles in the jet:

$$P = \sum_i p_i \ ,$$

closely mirrors the trajectory of the initial quark or antiquark. This correspondence stems from the phenomenon of asymptotic freedom in QCD, where interaction weakens significantly at short distances. Hence, the quark and antiquark only experience substantial interaction when they are separated by about 1 femtometer (1 fm), rendering only modest momentum transfer plausible. This, in turn, culminates in the formation of jets that largely align with the direction of initial quark and antiquark.

The way these jets spread out in relation to the electron beam direction, shows how the quark and antiquark in the basic $e^+ + e^- \rightarrow q + \bar{q}$ reaction is distributed in angles (Figure 1.8). Also, the angular distribution of these quarks can be conveniently calculated, aligning closely with the observed jet angular distribution. This congruence further bolsters the understanding of the inherent processes behind quark-antiquark generation and subsequent fragmentation in the context of electron-positron annihilation.

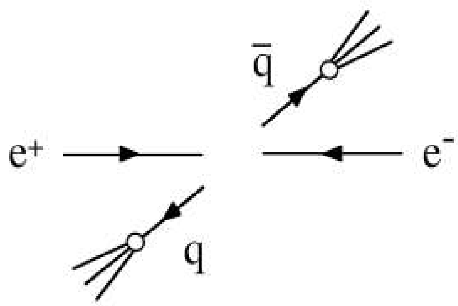

Figure 1.8. Visual representation of the formation of two jets in annihilation of electron-positron (https://www.semanticscholar.org/paper/Positron-electron-proton-Colliding-Beams-Lee-P./200442c714931ef83f007f750d3ccbc5871e5386/figure/3 [last access date: 24.08.2023])

Gluon Jets

Annihilation of electrons and positrons resulting in the formation of hadrons, usually involves the formation of two jets moving in opposite directions. However, at times, a high-momentum gluon may be released by the quark or antiquark before fragmentation, similar to how an energetic electron can emit a photon. In these scenarios, a three-jet event materializes, where the quark, antiquark, and emitted gluon each go on to form distinct sets of hadrons.

These instances of three-jet occurrences served as compelling evidence for the actual existence of gluons. The observation of jets angular distributions in these events matches what we expect for gluons with spin-1, confirming our theoretical predictions. However, they deviate from expectations associated with particles of spin zero, offering further substantiation for the gluon's presence.

Calculating the proportion of events with three jets compared to those with two jets, assuming the third jet is a gluon, reflects the influence of the fine structure constant (α) on the chance of an electron or positron emitting a photon. In this context, the probability of a quark or antiquark emitting a gluon hinges on the strong coupling constant (α_s). Remarkably, the calculated ratio harmonizes exceptionally well with the empirically measured value, fortifying the credibility of this interpretation.

The identification of three-jet incidents within electron-positron annihilation played an instrumental role in affirming the reality of gluons and providing robust support for the theoretical framework grounded in the fundamental attributes of the strong force.

1.4. The SM's Unsolved Mysteries

While the SM has achieved impressive success in explaining many phenomena and making accurate predictions, it does have some limitations and open questions. It presents several primary challenges and constraints such as:

Lack of Gravity: the SM does not include gravity as one of its fundamental forces. The General Relativity of Einstein aptly describes gravity and stands as a distinct theory from the SM.

At the quantum level, the SM showcases an exceptional precision in elucidating the actions of elementary particles and their interactions. However, it does not provide a framework to incorporate gravity, which is the force responsible for the interactions of massive objects in space-time. Gravity is significantly weaker than the other fundamental forces at the particle level, and it becomes more important at larger scales, such as in the interactions of celestial bodies. Attempts to combine gravity with the other forces and incorporate it into the framework of the SM have proven to be challenging. This has led to the pursuit of theories beyond the SM, such as *string theory* and *supersymmetry*, which aim to unify all the fundamental forces, including gravity.

The SM is a highly successful theory for describing the three non-gravitational fundamental forces but does not include gravity. The quest for a more complete and unified theory of all the fundamental forces, including gravity, remains an ongoing area of research in theoretical physics.

Dark Matter: one of the major challenges of the SM is the dark matter problem. Dark matter refers to a form of matter that does not emit, absorb, or interact with light or other electromagnetic radiation, making it invisible to direct observation. Observations suggest that dark matter makes up about 27% of the universe's mass-energy content, but its nature remains unknown. However, we deduce its existence through the gravitational effects it exerts on observable matter and its role in shaping the universe's extensive structure.

The presence of dark matter is a well-established astrophysical and cosmological phenomenon, but its nature remains among the paramount unresolved inquiries in contemporary physics. Understanding dark matter is an essential goal in current research, as it can provide crucial insights into the fundamental nature of the universe and may require extensions to the SM to fully explain its properties and interactions.

Dark Energy: similar to dark matter, the SM cannot explain dark energy, which is believed to be driving the observed accelerated expansion of the universe. It is important to note that dark energy is not directly incorporated into the SM itself. Instead, dark energy is a concept that arises in the context of cosmology and the study of the universe's large-scale behavior.

Neutrino Masses: the neutrino masses problem is another limitation of the SM. In its initial formulation, it was posited that neutrinos were massless particles. However, evidence from neutrino oscillation experiments has demonstrated that neutrinos possess minuscule yet non-zero masses.

Hierarchy Problem: the hierarchy problem, which relates to the large distinction between the electroweak scale (characterized by the masses of W and Z bosons) and the Planck scale (the energy level where gravity starts to exert notable influence.). The question is why these scales are so vastly different.

Matter-Antimatter Asymmetry: this observed lack of balance between matter and antimatter in the universe is widely referred to as the "baryon asymmetry problem."

As per the Big Bang theory, the universe is believed to have originated with an extremely high-energy and high-temperature state, where matter and antimatter were produced in equal amounts. In accordance with the principles outlined in the SM, particles and their corresponding antiparticles should have been formed in balanced quantities during the early universe.

When matter particles encounter their antimatter counterparts, they undergo mutual annihilation, converting their mass into energy in the form of photons. If the early universe had equivalent quantities of matter and antimatter should have annihilated completely, leaving behind only photons.

Naturalness Problem: the Higgs boson mass, as measured by experiments, is significantly lower than the expected value based on theoretical calculations, leading to the naturalness problem. This has raised questions about whether there are undiscovered particles or phenomena influencing the Higgs boson mass.

Strong CP Problem: the SM has a theoretical parameter called theta (θ) that, based on calculations, should be nonzero and lead to observable violations of charge-parity (CP) symmetry. However, experimental measurements indicate that CP violation is exceedingly small, and the reason for this discrepancy remains unknown.

Neutrino Oscillations: While the discovery of neutrino oscillations confirmed neutrino masses, the mechanism behind neutrino oscillations is not fully understood within the SM.

To address these limitations and open questions, physicists are actively working on extensions to the SM, such as supersymmetry, theories of everything and other. But they must to be proven experimentally to be accepted. For this purpose, many experiments have constructed around the world. For instance, Stanford Linear Accelerator Center (SLAC) is founded in 1962 in Menlo Park, California, United States. The location of the SLAC, spanning 3.2 kilometers, holds the distinction of being the planet's lengthiest linear accelerator. Functioning since 1966, it possesses the capacity to propel electrons to energy levels as high as 50 GeV.

The inception of the Fermi National Accelerator Laboratory (Fermilab) took place in 1967 within Chicago, United States, specializing in the domain of high-energy particle physics. Notably, Fermilab housed the Tevatron accelerator, boasting a circumference of 6.28 kilometers, which reigned as the globe's most potent particle accelerator from 1983 to 2011. This accelerator earned the distinction of being the first to achieve an energy level of one tera-electron-volt (TeV). It accomplished this feat by propelling protons and antiprotons to energy thresholds of 980 GeV, culminating in proton-antiproton collisions that reached energies up to 1.96 TeV. LHC at CERN commenced operations in 2008, succeeding the Tevatron as the pinnacle particle accelerator.

1.5. CERN and the LHC

Figure 1.9. CERN, the European Organization for Nuclear Research
(https://visit.cern/ [03.06.2023])

CERN, the largest on a global scale intergovernmental particle physics laboratory, was established in 1954. It is situated near Geneva, at the border of France and Switzerland. The satellite view of CERN is shown in Figure 1.9. CERN's primary objective is to provide the necessary infrastructure, including particle accelerators, for high-energy physics research. By means of international collaborations, several experiments have been conducted at CERN. The LHC, renowned as the most extensive and energetically potent particle collider and accelerator worldwide, underwent construction from 1998 to 2008. This colossal endeavor entailed the concerted efforts of numerous scientists, hundreds of educational institutions and research facilities, alongside the active involvement of over 100 nations. The LHC resides in a 27-kilometer tunnel, reaching depths of up to 175 meters. Four experiments, denoted as CMS, ATLAS (A Toroidal LHC Apparatus), ALICE (A Large Ion Collider Experiment) and LHCb (LHCbeauty) are strategically stationed along this expansive collider. There are indeed four more smaller experiments positioned at the LHC such as Monopole and Exotics Detector at the LHC, Total Cross Section, Elastic Scattering, and Diffraction Dissociation Experiment, LHCforward, and ForwArd Search ExpeRiment, each investigating particle collisions from different perspectives using diverse technologies.

It operates based on the principles of electromagnetism and uses superconducting magnets to guide and propel particles to velocities approaching the speed of light. The LHC has been designed for the purpose of colliding proton or heavy ion beams at extremely high energies, allowing scientists to study fundamental particles and their interactions in unprecedented detail.

1.5.1. The Mechanism of Working for the LHC

1. *Accelerating Protons:* The LHC uses a series of pre-accelerators to bring protons up to high energies before they enter the main collider. Protons are initially obtained from hydrogen gas and accelerated by a linear accelerator LINAC 2. Subsequently, they pass through the Proton Synchrotron , the Super Proton Synchrotron , and finally enter the LHC.
2. *Proton Beams*: The LHC is composed of two distinct beam pipes, each capable of holding and guiding a proton beam in opposite directions. These beams are circulated in the collider ring, which has a circumference of about 27 kilometers.
3. *Superconducting Magnets*: The LHC uses superconducting magnets to bend and steer the proton beams along their circular path. These magnets are kept at extremely low temperatures using liquid helium to maintain their superconducting properties, allowing for a very high magnetic field strength.
4. *Collision Points*: The LHC features primarily four intersection points, namely ATLAS, CMS, ALICE, and LHCb. At these points, two streams of particles are deliberately collided. These intersections serve as the designated locations for particle detectors, positioned to meticulously observe and document these collisions.

At these specific junctures, the proton beams are deliberately directed to collide, releasing a tremendous amount of energy that produces a wide variety of particles, including rare and short-lived particles.

5. *Particle Detectors:* The detectors located at the collision points are enormous and complex instruments designed to capture and analyze the products of the proton collisions. They are crucial for recording the particles and their energies, allowing scientists to study the resulting debris and interactions.
6. *Studying Particle Interactions:* When the protons collide, they release a tremendous amount of energy, producing a variety of particles, including rare and short-lived particles that could potentially unlock insights into the fundamental essence of matter and the universe.
7. *Data Analysis:* The information amassed from the detectors is massive and requires sophisticated computing infrastructure and algorithms for analysis. Researchers meticulously analyze the data to investigate the characteristics of established particles, explore novel particles, and assess theories encompassing both SM predictions and those extending beyond it.

The LHC has played a pivotal role in achieving groundbreaking advancements in particle physics, exemplified by its pivotal role in the landmark discovery of the Higgs boson in 2012. Continuously, it stretches the limits of our comprehension regarding fundamental particles and their interactions, illuminating the enigmatic corners of the universe.

1.6. CMS

The CMS experiment stands as a paramount and expansive endeavor within the framework of the LHC.

CMS is essential for finding out more about the Higgs boson, which is a special particle predicted by scientists. It also helps us understand other mysteries in particle physics, like extra dimensions and the stuff called dark matter. To do even better science, the CMS experiment is getting an upgrade called the HGCAL. This upgrade helps to deal with the challenges of radiation and lots of events happening at once. With HGCAL, CMS can study the little details of the particle showers, which helps in identifying particles better and improving the accuracy of the measurements.

The CMS experiment stands as a colossal collaborative undertaking, uniting thousands of scientists, engineers, and researchers hailing from diverse corners of the globe. Their collective dedication is channeled towards unraveling the elemental constituents of the universe and unraveling the enigmas concealed within the cosmos.

Within the confines of this thesis, I will engage deeply in the domain of data analysis simulation concerning the HGCAL, which constitutes a significant aspect of my research. The utilization of HGCAL data analysis simulation allows for a comprehensive investigation into the behavior and characteristics of particle showers, leading to enhanced particle identification, improved energy resolution, and more effective Pile up (PU) rejection. Throughout this study, I aim to shed light on the intricacies of particle interactions, paving the way for a more profound comprehension of the fundamental components of the universe and contributing to the advancement of particle physics research.

2. PRELIMINARY WORK

The LHC conducted proton-proton collisions at various energies, including $\sqrt{s} = 7$ TeV and $\sqrt{s} = 8$ TeV during Run 1 (2010–2012), and $\sqrt{s} = 13$ TeV during Run 2 (2015-present). During Run1, the Higgs boson was discovered. Run 2 aims to accumulate about 300 fb^{-1} [2] of data by 2023, and the High-Luminosity LHC (HL-LHC) phase is planned to begin in 2026, targeting 3000 fb^{-1} by the mid-2030s. HL-LHC will have higher luminosity but will pose challenges related to radiation tolerance and the handling of event PU within detectors. To address these challenges, the CMS Collaboration proposes the replacement of current endcap calorimeters with the HGCAL, ensuring better physics performance for future experiments. Prior to commencing the discussion on HGCAL, it is pertinent to introduce the CMS detector, as it serves as a foundational framework for comprehending the underlying mechanisms of HGCAL.

2.1. CMS Detector

The CMS is like a giant camera that looks at the particles produced when protons collide at very high speeds. The main goal of the CMS experiment is to explore and study various aspects of

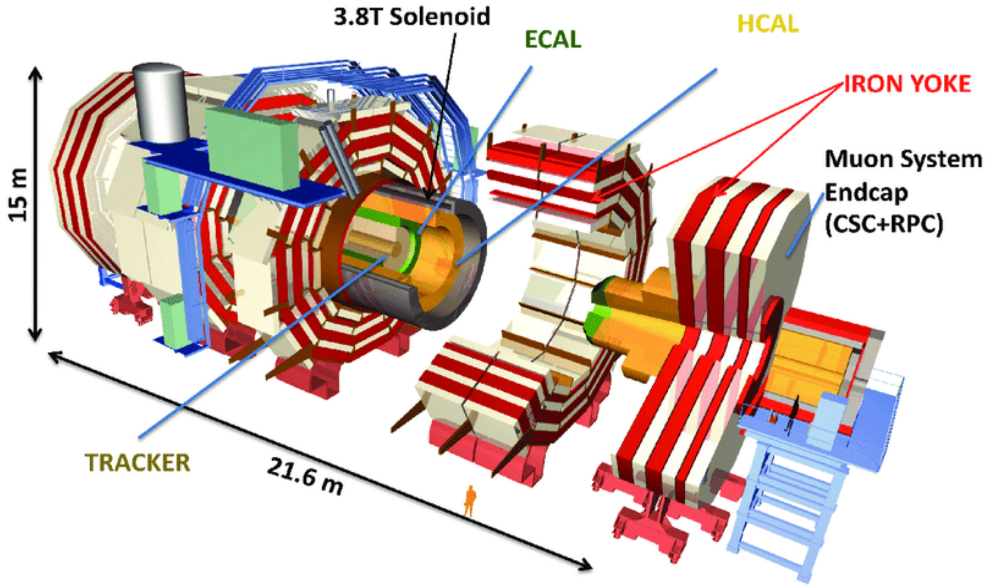

Figure 2.1. Internal composition of CMS. It consists of various components, including the barrel, where a person can be seen for scale reference. The barrel region is surrounded by the HCAL and ECAL. They are designed to calculate the energy of hadrons and electromagnetic particles like electrons and photons, respectively. This setup allows CMS to detect and measure produced particle as a result of in high-energy collisions at the LHC. (https://cms.cern/detector [last access date : 15.06.2023])

[2] A femtobarn is a unit used to measure cross-section, which quantifies the likelihood of a particular event happening during a particle interaction.

particle physics. The experiment is positioned at one of the four major collision points in the LHC. When the protons smash into each other, they release a lot of energy, creating a shower of different particles. The CMS detector captures these particles and records their properties, like their energy, momentum, and type.

The CMS detector has a hollowed cylinder shape and is partitioned into a central barrel and terminal end-cap sections which is shown in Figure 2.1. It comprises various sub-systems, such as the superconducting solenoid that produces a consistent magnetic field aligned with the beam and encompasses the majority of the detector components. Other sub-systems include the tracking sub-system for measuring particle momentum and energy, calorimeters for energy measurements, and the muon system positioned beyond the solenoid, designed to gather data pertaining to muons.

2.1.1. Structure and Function

The CMS detector, weighing 14,000 tons, derives its name from its compact size compared to the amount of detector material it holds. Standing at 15 meters high and 21 meters long, it is uniquely designed to accurately detect muon particles. The key to its precision lies in the powerful solenoid magnet, the most potent of its kind ever built.

The CMS detector's structure resembles that of an onion, with multiple concentric layers of components. Each of these components plays a crucial role in capturing valuable data from collision events. They work together to create "photographs" of each collision by analyzing the characteristics and properties of the particles produced during the event. This comprehensive analysis helps in unraveling the underlying physics of the collisions.

The Role of Powerful Magnets in the CMS Detector

The CMS detector contains a powerful magnet known as the *solenoid*, which plays a crucial role in bending charged particles as they emerge from collisions. This is shown in Figure 2.1. This bending serves two purposes: determining the charge (positive or negative) of the particles and measuring their speed or momentum. The solenoid is made of special coils that, when electricity flows through them, create a very strong magnetic field much stronger than the Earth's magnetic field. To contain this powerful magnet, a heavy steel cover surrounds it. Despite its weight, this solenoid is the largest of its kind and allows the CMS detector to maintain a compact and efficient design.

Track Identification in CMS

Track identification is a crucial process in the CMS experiment, as it enables the reconstruction of the paths taken by charged particles produced in high-energy collisions. This information is vital for understanding the behavior of particles at the collision point.

The CMS detector employs a sophisticated silicon Tracker, consisting of approximately seventy-five million electronic sensors organized in successive circular layers. As charged particles traverse through the Tracker, they interact with the silicon sensors, leaving behind hits or signals. These hits are carefully recorded, and sophisticated algorithms are employed to combine them, accurately reconstructing the trajectories of the particles' paths.

The Tracker possesses the capacity to discern high-energy muons, electrons, and hadrons, includes the paths originating from the decay of temporary particles like beauty or b quarks. This attribute is especially notable, as it facilitates the exploration of distinctions between matter and antimatter. To achieve precise results without unduly affecting the particles' paths, the Tracker needs to be lightweight and radiation-resistant. It accomplishes this by employing silicon sensors that provide fast response and excellent spatial resolution, allowing for reliable track reconstruction with just a few measurement points.

In the center of the CMS detector, the tracker handles the most particles. This structure is composed of a dual composition—pixels at its nucleus, adept at managing the heightened particle density, encircled by silicon microstrip detectors. These silicon components generate minuscule electrical signals, subsequently amplified, identified, and transformed into pulses. Following this process, the data is transmitted via fiber optic cables to be scrutinized within a radiation-free setting.

The Tracker employs a large number of electronic readout channels, with silicon sensors covering an area equivalent to that of a tennis court. This vast coverage enables efficient detection of numerous particles within a confined space.

The CMS Tracker has been operational since its installation in late 2007, playing a crucial role in providing valuable data for understanding the particles' properties and interactions in high-energy collisions.

Measuring Energy

Understanding the energies of particles produced in collisions is essential in studying what happens at the collision point. CMS uses two types of "calorimeters" to gather this information. The Electromagnetic Calorimeter (ECAL) measuring the energy of electrons and photons with bringing their motion to a complete stop. Conversely, the Hadron Calorimeter (HCAL), positioned beyond the ECAL, intercepts hadrons. In synergy, these calorimeters furnish crucial information about particle energies and interactions at the collision point.

ECAL

The role of the CMS ECAL is to measure the energies of electrons and photons. Functioning effectively within the demanding LHC conditions, marked by a strong magnetic field, high radiation levels, and short time intervals between collisions, necessitates specialized detector materials. The utilization of lead tungstate crystal in the ECAL is due to its distinctive attributes. This crystal is transparent and emits light (scintillates) when electrons and photons traverse it, enabling precise energy measurement. The high-density nature of these crystals generates light in brief, well-defined bursts, resulting in a rapid and compact detector.

Photodetectors, designed to function in high magnetic fields, are affixed to the crystals to detect the scintillation light. They transform the light into electrical signals, which are subsequently amplified and scrutinized.

The ECAL is segregated into a central "barrel" segment and two "endcaps." It is illustrated in Figure 2.2. The barrel encompasses 61,200 crystals organized into 36 super modules, while the endcaps feature nearly 15,000 additional crystals.

To enhance precision, a pre-shower detector is incorporated in front of the endcaps within the ECAL. This component aids in distinguishing between individual high-energy photons, indicative of compelling physics events, and less significant pairs of low-energy photons.

In essence, the CMS ECAL comprises approximately 80,000 lead tungstate crystals, each weighing 1.5 kg but occupying a volume similar to that of a small coffee cup. The growth process for each crystal spans around two days.

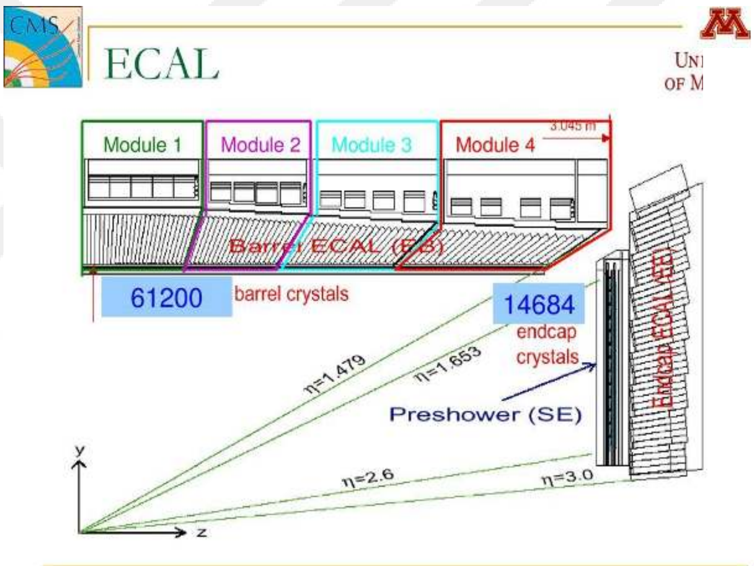

Figure 2.2. CMS ECAL structure (CMS Collaboration , 2018, The Phase-2 Upgrade of the CMS endcap calorimeter, Technical Design Report, CMS-TDR-019)

HCAL

The HCAL holds a critical role within the CMS detector, that measures the energy of particles known as "hadrons," including protons and neutrons, which are composed of quarks and gluons. It also indirectly detects uncharged particles like neutrinos. Measuring these particles is vital for understanding the formation of new particles like the Higgs boson or supersymmetric particles.

To capture all particles, including those that produce new ones not directly detectable, the HCAL is designed to be "hermetic." It has staggered layers to prevent any gaps where familiar particles might escape. The HCAL is designed as a "sampling calorimeter" featuring alternating layers of "absorber" and "scintillator" materials. It measures position, energy, and arrival time of a particle by detecting the fast light pulse produced when the particle passes through the layers.

The HCAL is large and thick, posing challenges to fit it into the compact CMS. It is structured into barrel (HB and HO), endcap (HE), and forward (HF) segments. It is illustrated in Figure 2.3. The HCAL uses unique materials and techniques to ensure it can withstand radiation and accurately measure particle energies.

Fun facts about the CMS HCAL: it uses old brass shell casings, each wedge is as heavy as six African elephants, and American high school students made over 400 "optical decoder" units.

Detecting Muons

The CMS detector's primary task is to detect muons, which are heavy charged particles like electrons but 200 times heavier. Muons are crucial in studying new particles, like the Higgs Boson, which can undergo a decay process resulting in the production of four muons.

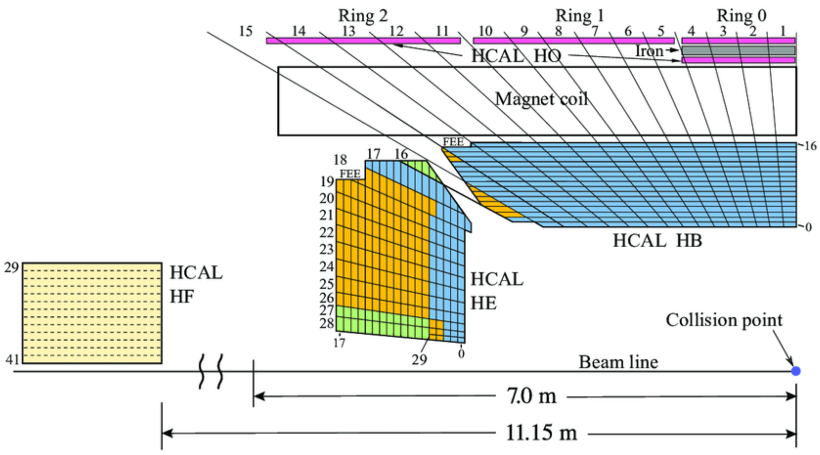

Figure 2.3. The HCAL structure (CMS Collaboration, 2018, The Phase-2 Upgrade of the CMS endcap calorimeter, Technical Design Report, CMS-TDR-019)

Unlike most particles, muons can pass through thick materials with little energy loss, making them unaffected by the calorimeters in CMS. For the detection of muons, dedicated chambers are positioned in the outer part of the experiment, as they are most likely to generate a distinct signal. To measure a muon's path and momentum, its position is tracked through multiple layers of the muon stations, combined with data from the CMS silicon tracker. The strong magnetic field generated by the CMS solenoid deflects the trajectory of muons, allowing scientists to determine its momentum.

CMS has a total of 1400 muon chambers, including drift tubes and cathode strip chambers for tracking and triggering, as well as resistive plate chambers and gas electron multiplier chambers for redundant triggering. This robust system effectively filters out background noise and ensures accurate data collection. Figure 2.4 shows a muon following a curved path in four layers of muon detectors.

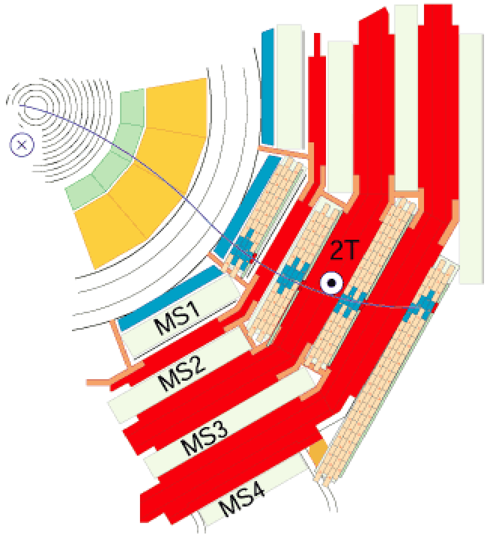

Figure 2.4. A muon, within the plane perpendicular to the LHC beams, follows a curved path as it passes through four layers of muon detectors, often referred to as stations (https://cms.cern/detector/detecting-muons [last access date : 17.07.2023])

The CMS detector was constructed in 15 separate sections or "slices" above ground and then lowered as ready-made units into the underground cavern. This strategy facilitated concurrent efforts in both cavern excavation and detector construction, resulting in time savings. Precise planning of cabling, piping, and slicing enabled seamless opening and closure of sections with minimal interruption, enhancing maintenance feasibility. Additionally, the distinct requirements of the LHC environment played a pivotal role in shaping the design of each detector layer.

2.2. HGCAL

The HGCAL holds significant importance in contemporary particle physics investigations as a fundamental element, meticulously crafted to gauge and identify the energy of particles generated during high-energy collision experiments. It is a critical part of several particle detectors, including those at the LHC and other future colliders.

The central objective of the HGCAL revolves around quantifying the energy of high-energy particles, encompassing electrons, photons, and various types of hadrons, which encompass both charged and neutral particles. This measurement is crucial for understanding the properties of these particles, as well as for discovering new particles and testing theoretical models.

The HGCAL uses a technique known as "calorimetry" to perform its energy measurements. Calorimeters work based on the principle that particles traveling through a medium will deposit their energy, producing a cascade of secondary particles. Subsequently, these secondary particles engage with the surrounding medium, triggering further particle generation and subsequent energy deposition. This process continues until the energy of the original particle is fully absorbed by the medium.

When a high-energy particle passes through the HGCAL, it interacts with the material, creating an "electromagnetic shower" for electrons and photons or a "hadronic shower" for hadrons. The shower development and energy deposition produce signals that are detected by the sensitive elements in the HGCAL, such as photodetectors in the case of lead tungstate crystals or electronic readouts for silicon sensors.

By analyzing the signals from the finely segmented HGCAL, physicists can reconstruct the energy and direction of the original particle with high precision. This information is crucial for identifying the particle type, distinguishing between different particles, and accurately measuring their momenta.

The HGCAL's high granularity is particularly important for distinguishing closely spaced particles and for precisely reconstructing the energy of particles with complex shower development patterns. Additionally, the high granularity helps in reducing the impact of PU events, where multiple particles are produced in the same collision, making it difficult to disentangle their individual contributions.

HGCAL is a important tool for particle physicists for the investigation of particle behavior at elevated energy levels, search for novel phenomena surpassing the boundaries of the SM, and improve our understanding about fundamental entities of the universe. As technology advances, the HGCAL continues to be refined and developed, playing a crucial role in future particle physics experiments and discoveries. The general view of HGCAL is shown in Figure 2.5.

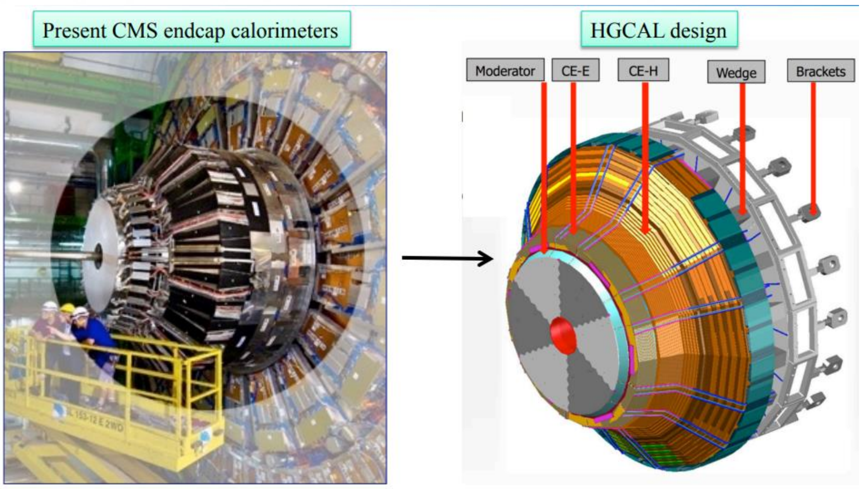

Figure 2.5. The HGCAL design (CMS Collaboration , 2018, The Phase-2 Upgrade of the CMS endcap calorimeter, Technical Design Report, CMS-TDR-019)

2.3. HGCAL Design Overview

The HGCAL is a new type of calorimeter that will be used in the CMS experiment. It will cover a specific region in the detector, specifically the area where particles are moving with a certain angle, between 1.5 and 3.0 .

The HGCAL is divided into two sections: the electromagnetic section and the hadronic section. These sections are named CE-E and CE-H, respectively. It is shown in Figure 2.6. Each section uses different materials in its layers to do its job.

To keep the HGCAL working properly, the entire system will be cooled down to a temperature of −30°C. This cooling is necessary to reduce electronic noise caused by current leaks and to make sure that the system continues to work well even after being exposed to radiation.

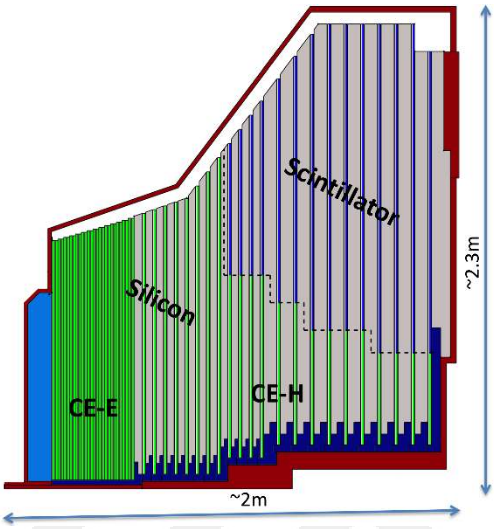

Figure 2.6.Material design for HGCAL (https://cds.cern.ch/record/2797452/files/OverviewDrawing_October2019.png [last access date: 17.10.2023])

2.3.1. Silicon Sensors

The HGCAL silicon sensors are designed to be simple and cost-effective, using as much space as possible on the circular wafers. To achieve this, the sensors are hexagonal in shape, with some tips trimmed off.

Initially, only sensors on 6-inch wafers were available, and they were considered as the starting point in the project. But now, 8-inch sensors are the preferred choice for the HGCAL. To qualify the full-size 8-inch sensors, an irradiation campaign will be conducted. This campaign includes measurements to optimize inter-pad capacitance and resistance, as well as noise measurements and laser tests on irradiated sensors. Hexaboards with integrated pogo-pins will be used to quickly connect the bare sensors to readout electronics.

Sensor Characteristics and Arrangement

In the CE-E and inner sections of the CE-H, the silicon sensors adopted are designed with planar DC-coupled hexagonal shapes. This choice of hexagonal design optimally utilizes the circular wafers, minimizing wastage compared to square or rectangular sensors by reducing unutilized space at the edges. The hexagonal sensors are tailored with trimmed corners, enhancing the wafer's surface utilization and facilitating the mounting system.

Through a comprehensive comparison of design alternatives, it was discerned that the adoption of hexagonal sensors yields significant cost reduction by optimizing silicon wafer usage. To enhance charge collection and sustain high performance across the operational lifespan of the HGCAL.

For the primary sensors, the chosen material consists of physically thinned p-type FZ silicon wafers for the 300 μm and 200 μm thick sensors. As for the 120 μm thick sensors, an alternative option entails p-type epitaxial material on a handle wafer. P-type sensors are favored due to their intrinsic robustness against non-Gaussian noise arising from radiation-induced effects. However, the use of n-type 300 μm sensors in the lower fluence part of HGCAL is being considered as it might lead to cost savings.

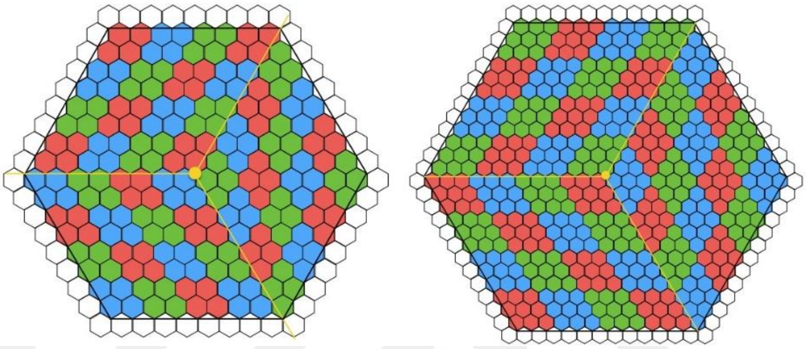

Figure 2.7. Sensor cells in a three-fold diamond pattern on PCB (CMS collaboration , 2018, The Phase-2 Upgrade of the CMS endcap calorimeter, Technical Design Report, CMS-TDR-019)

The "three-fold diamond" configuration was chosen for the sensor cells, enabling symmetric configurations of neighboring cells to assemble into trigger primitives. This configuration simplifies the module layout and readout printed circuit board (PCB) design. The Figure 2.7 illustrates the arrangement of sensor cells in a three-fold diamond pattern on hexagonal 8-inch silicon wafers. On the left side, the larger sensor cells can be seen , which cover an area of 1.18 cm^2. These cells are grouped together and summed to form trigger cells. On the right side, there is smaller sensor cells, which cover an area of 0.52 cm^2. Similarly, these small cells are also grouped and summed to create trigger cells. This configuration allows for convenient grouping and organization of the sensor cells, making it easier to form trigger primitives for the system.

The PCB (is shown in Figure 2.8) accommodates four SKIROC2-CMS front-end readout chips and an FPGA, which are utilized during beam testing. To allow access to the mounting holes on the baseplate, the corners of the PCB and the underlying sensor have been removed. The hexagonal silicon sensors offer cost savings and efficient use of the wafers, with different thickness options to optimize performance. The choice of p-type sensors is preferred, but n-type sensors are also being studied for specific areas. The three-fold diamond configuration is selected for its ease of design and readout implementation.

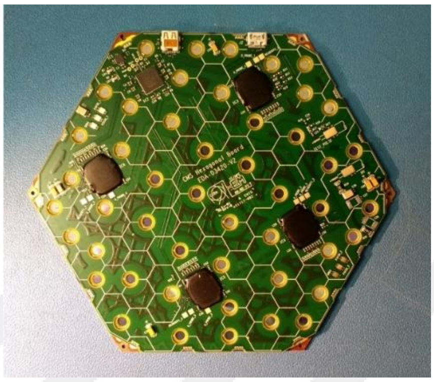

Figure 2.8. Pre-wirebonding and encapsulation: six-inch module on carrier plate (CMS collaboration, 2018, The Phase-2 Upgrade of the CMS endcap calorimeter, Technical Design Report, CMS-TDR-019)

Sensor Production

To reduce risks in producing 600 $m^2$of silicon sensors for the HGCAL project, a similar dual-source strategy, as used by CMS and ATLAS Tracker sensor productions, is being pursued. The qualification process for suitable companies has begun through a CERN market survey. Three potentially suitable companies have been identified, matching the required profile for producing 8-inch HGCAL sensors. These companies will undergo further technical evaluation.

Several 6-inch and 8-inch sensors have been received, but the focus is on the 8-inch sensors for the HGCAL project. HPK, the company involved, has implemented the technology for producing 8-inch sensors and has delivered full-size 8-inch demonstrator sensors with similar design and characteristics to the required HGCAL sensors.

The demonstrator sensors show that the quality achieved in the 8-inch production lines is comparable to that of the established 6-inch production lines. Initially, a 'stepper' technique for photolithography was used, which limits the geometry of the cell and periphery. However, for large-scale production, HPK will use a full-wafer lithography process, which provides excellent photolithography and is consistent with the specifications used for 6-inch sensor production. HPK is confident that this change in process will not affect the resulting sensor quality and characteristics.

2.3.2. Silicon Modules

The HGCAL requires approximately 27,000 silicon detector modules to complete its CE-E and CE-H segments. A CE-E module is comprised of several components, including a baseplate, a Kapton-gold sheet, a silicon sensor, and a hexaboard equipped with front-end electronics.

The effectiveness of the mechanical design was confirmed through the examination of 8-inch module mockups, which displayed satisfactory thermal contact when pressed onto the cooling surface. Calculated stresses on the modules were significantly below the threshold of breakage.

Initial testing employed 6-inch modules, as depicted in Figure 2.9, showcasing a fully assembled 6-inch module. For CE-E, the baseplate is fashioned from a sintered WCu metal matrix composite, ensuring excellent thermal conductivity. CE-H utilizes a high-thermal-conductivity carbon fiber baseplate, although it doesn't contribute substantially to CE-H absorber functionality.

The WCu baseplates feature a consistent thickness of 1.40±0.03 mm, exhibiting faces with flatness within ±50 µm. A Kapton foil, 105 µm in thickness and coated with a delicate layer of gold, is bonded to the baseplate, granting electrical insulation and a HV bias connection.

Hexagonal in shape, both the silicon sensors and hexaboard possess small corner cutouts that facilitate access to mounting holes and connections. The hexaboard integrates HGCROC front-end readout ASICs for signal digitization. Through epoxy bonding, the baseplate, Kapton layer, silicon sensor, and hexaboard are amalgamated into a unified unit. Wirebonds link the hexaboard with each sensor pad, the Au-Kapton layer, and sensor guard rings. These wirebonds are safeguarded with a clear, radiation-tolerant silicon elastomer.

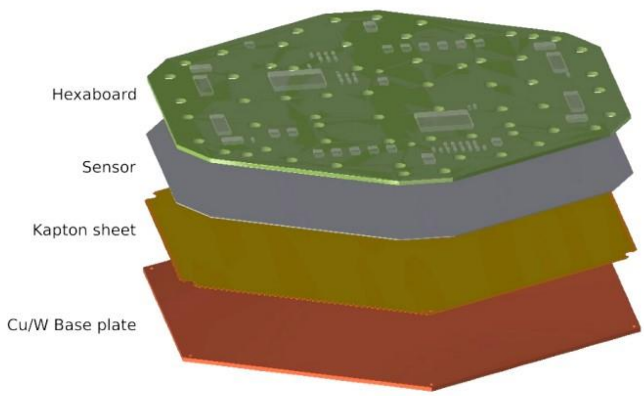

Figure 2.9. The CE-E silicon module consists of multiple layers stacked together (CMS collaboration , 2018, The Phase-2 Upgrade of the CMS endcap calorimeter, Technical Design Report, CMS-TDR-019)

2.3.3. Plastic Scintillators

The impact of ionizing radiation on the current HE (Hadronic Endcap) has been extensively studied using various methods like UV-laser excitation, radioactive sources, and beam data. These studies reveal that the damage to the scintillator depends on the dose rate, with lower dose rates causing more damage due to scintillator chemistry and oxygen diffusion effects. Although plastic scintillator has been used at low temperatures in space-based experiments, its radiation tolerance and dose-rate dependence at such temperatures haven't been thoroughly investigated before.

The Figure 2.10 illustrates the relationship between the dose constant, denoted as Dc, and the dose rate, represented by R. The dose constant Dc is a measure of the dose at which the light output diminishes by a factor of e. It can be seen there is two lines: one corresponds to D_c=3.6 x $R^{0.5}$ and the other to D_c=2.5 x $R^{0.5}$.

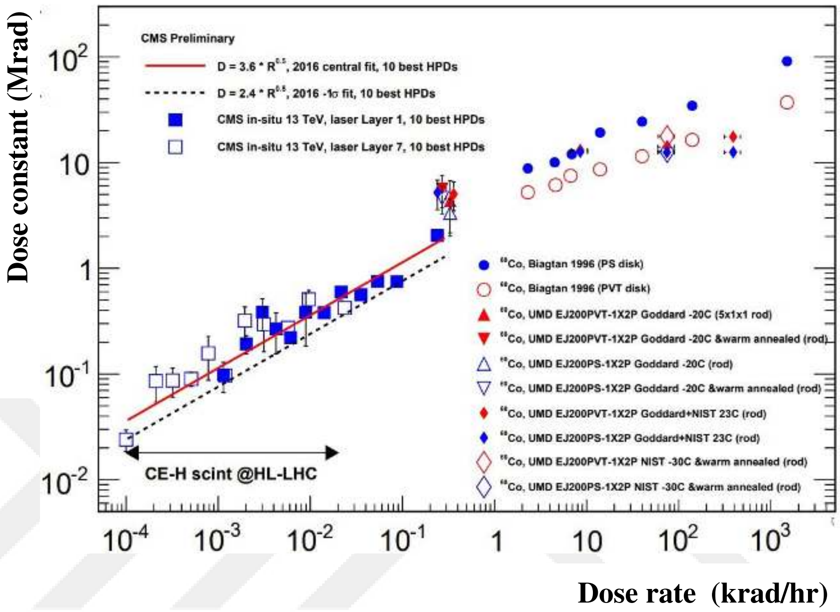

Figure 2.10. Relationship between the dose constant and the dose rate. (CMS collaboration , 2018, The Phase-2 Upgrade of the CMS endcap calorimeter, Technical Design Report, CMS-TDR-019)

The figure displays measurements from the existing HE detector using square symbols based on data collected during 2016. Other points are from dedicated studies conducted in irradiation facilities, including low-temperature irradiations. The consistency between scintillator performance at room temperature and low temperature is demonstrated by the points clustered around 0.3 krad/hr. To predict performance, the data is fitted to a specific function as below by Eq (2.1).

$$D_c = 3.6\,Mrad\left(\frac{R}{1krad/hr}\right)^{0.5} \qquad (2.1)$$

The data is fitted with a red line in the figure, and the variable R represents the dose rate in krad/h.

There are two types of scintillator materials that can be used for this purpose. The first one is *polyvinyl toluene-based (PVT)* scintillator, which is available from different suppliers like EJ-200 from Eljen or BC-408 from Saint-Gobain. The second type is *polystyrene-based (PS)* scintillators, which can be economically produced using injection-moulding techniques.

These lines are used to fit the data points and represent the trend observed in the measurements. This measurement is specifically related to SCSN81, a type of plastic scintillator employed in the endcaps of the present detector. The data and lines in the figure provide valuable insights into the relationship between dose constant and dose rate for this scintillator material.

To make the best choice, various factors will be taken into consideration, including cost, performance after exposure to HL-LHC, and the ease of assembly. All these factors will determine which scintillator material is the most suitable for the project.

2.3.4. SiPM photodetectors

The scintillation tiles will produce light that is then detected by SiPM photodetectors. These photodetectors possess a high gain, exceeding 10^5, and demonstrate exceptional efficiency, surpassing 30%, in capturing light signals. Rigorous investigations have been conducted to assess their performance, stability, and responsiveness to radiation.

The SiPMs used in the Phase-1 HCAL upgrade serve as a reference for the scintillator part of the endcap calorimeter upgrade. The specifications for the SiPMs in the endcap calorimeter draw heavily from those of the Phase-1 HCAL SiPMs, although certain adjustments have been made due to variations in the SiPM-on-tile arrangement, where each individual cell is independently read.

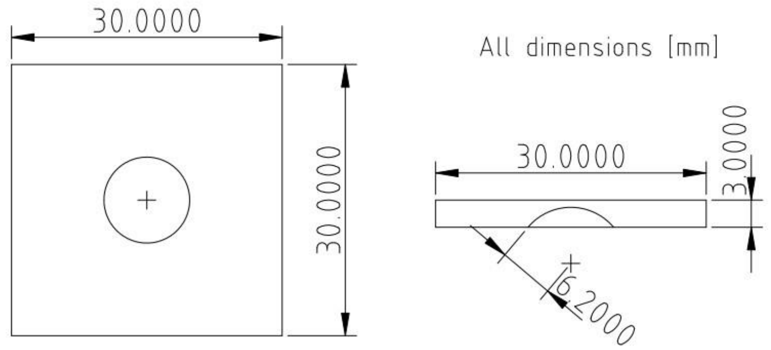

Figure 2.11. The CALICE Collaboration has developed typical square tiles as shown in the parameter drawing. However, for the CMS endcap calorimeter, the tiles will be ring-sections instead of squares, as this design is better suited to the endcap's geometry. (CMS collaboration, 2018, The Phase-2 Upgrade of the CMS endcap calorimeter, Technical Design Report, CMS-TDR-019)

SiPMs have a fixed number of pixels that can make them nonlinear, but these nonlinearities can be predicted and corrected for, especially when each tile is read separately. The dark current of SiPMs increases after irradiation, and this noise rate is linear with the neutron fluence. The noise rate is also temperature-dependent but to a lesser extent than unity-gain devices like PIN diodes.

For signal reconstruction, what matters most is the statistical fluctuation of the number of pixels firing, which depends on the dark current, provided that the cell-to-cell crosstalk is minimal.

The detector design has two main goals: first, it must allow calibrating individual tiles using particles with minimum energy; second, it should be compact and not use too much space at the edge. After considering different options, they chose the SiPM-on-tile technology, which reads light from the scintillator tile directly using a small dimple for mounting the SiPM. This design is cost-effective and provides good performance for particle tracking and identification. Figure 2.11 and Figure 2.12 depict a standard square tile developed by CALICE, with both a drawing and a photograph showcasing its design. An example of three CALICE scintillator tiles, each measuring 3 × 3 cm², is shown in the Figure 2.12. They are mounted on a printed circuit board (PCB), with one SiPM per tile. In the left two scintillators, The SiPM is placed in the small dome at the center of each tile, with the tile on the rightmost side being enveloped by reflective foil. The reflective foil helps improve light collection efficiency by bouncing the light back towards the SiPM.

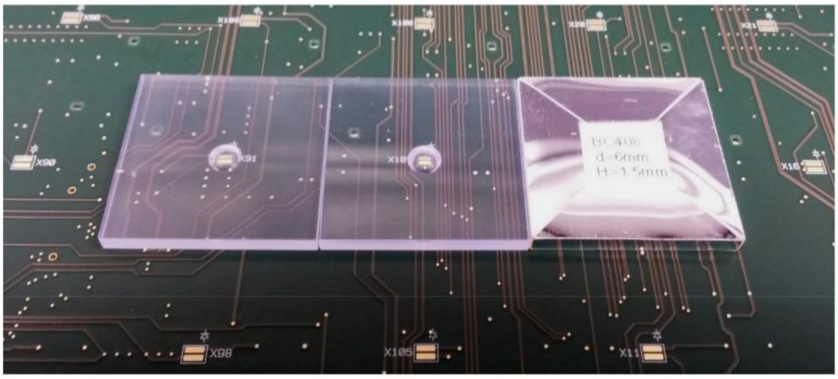

Figure 2.12. Three CALICE scintillator tiles affixed to a PCB (CMS collaboration , 2018, The Phase-2 Upgrade of the CMS endcap calorimeter, Technical Design Report, CMS-TDR-019)

2.4. Reconstruction in HGCAL

A special software framework called CMSSW was created for analyzing the data from the HGCA beam experiments. This software processes the data acquired from the HGCAL Data Acquisition System in a specific format and processes it to produce analyzed objects that researchers can use for their analysis.

Additionally, depending on the noise conditions during different beam periods, various strategies can be applied to the data, leading to different reconstruction approaches. This flexibility allows for more accurate analysis based on the specific conditions during each beam period.

2.4.1. Simulation

The detector geometry for the HGCAL was frozen in 2016 to proceed with simulation work. It consists of several layers: the EE is an Electromagnetic section with a depth of about 1.5 λ, followed by the FH, a Hadron section with a depth of 3.5 λ, and the BH, a Backing section with a depth of 5 λ. These layers are made of various materials, including silicon and stainless steel. The EE has 28 active layers, while the FH and BH each have 12 active layers.

The simulation of signal development and processing in the HGCAL electronics includes the addition of Gaussian noise and digitization. The noise levels vary depending on the cell size and the type of sensor used. The detector design aims to use 120 µm sensors in the region with high neutron fluency, resulting in lower noise levels compared to using 100 µm sensors.

2.4.2. Clustering

In the initial reconstruction prototype, a two-dimensional 2D clustering algorithm is employed to identify localized energy concentrations in each layer of the calorimeter. By setting an energy threshold for cells, we calculate the energy density based on the neighboring cells. Cells with high density and proximity form new clusters, while remaining cells are associated with the nearest cluster, aiding in the separation of energy clusters resulting from showers.

Next, the layer clusters are gathered to construct three-dimensional clusters (multiclusters) by associating layer clusters from different layers aligned approximately in a linear path starting at the center of the CMS detector. For multiclusters used in forming electron and photon candidates, a 2 cm alignment requirement is applied. The layer clusters used for multiclusters are marked as used and not considered for further cluster formation.

Finally, the multiclusters are integrated into the existing CMS Particle Flow (PF) system for further analysis and interpretation, accurately reconstructing the particles and their properties.

2.5. Jet reconstruction

To better understand the HGCAL's performance, studies were conducted using standard jet algorithms. These algorithms assist in directly collecting the energy of quark jets calculated from the separate reconstructed hits. The distance parameter, R, of the anti-k_T algorithm was varied to assess the impact of PU on the results.

Figure 2.13 (left) displays the transverse energy per unit area (in η, φ space) for different PU conditions. Pure PU events show noticeable energy deposits, reaching about 200 GeV with approximately 200 PU interactions every bunch crossing. Comparing energy distributions between quark jets and PU jets, it is observed that PU jets have more energy deposited in the earlier part of the calorimeter, likely due to softer particles in PU.

In Figure 2.13 (right), a comparison is made between the amount of transverse energy deposited in each layer of the calorimeter for quark jets (with ET = 50 GeV, and $2 < |\eta| < 2.5$) and PU jets. Quark jets show a narrower shape compared to the broader energy distribution observed in PU jets, particularly noticeable in the EE.

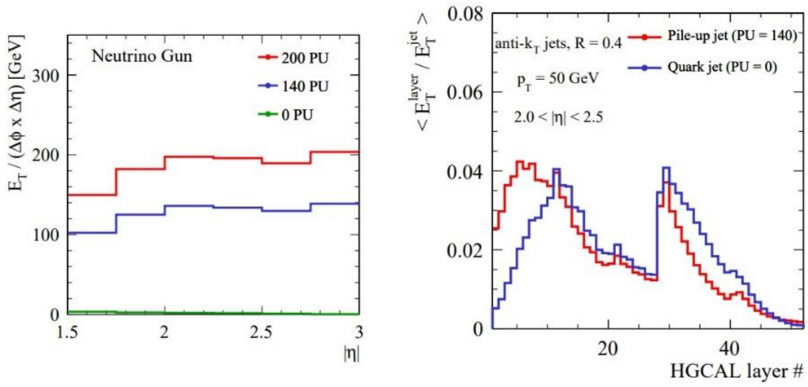

Figure 2.13.The diagram on the left shows the distribution of transverse energy per unit area in the η-φ space. The figure on the right illustrates the transverse energy deposited as a function of the calorimeter layer. (CMS collaboration, 2018, The Phase-2 Upgrade of the CMS endcap calorimeter. Technical Design Report, CMS-TDR-019)

Figure 2.14. illustrates the lateral energy containment as a function of radius for different sections of the calorimeter: EE, the first 12 layers of the FH, and the last 12 layers of the BH. The narrower profile of quark jets compared to PU jets is clearly visible, especially in the electromagnetic section.

In the left plot, we see the radial profile for the EE of the calorimeter. The blue histogram represents quark jets, and the red histogram represents jets originating from PU interactions. The plot shows how the energy of the quark jets is distributed across the layers, starting from the center and moving outward.

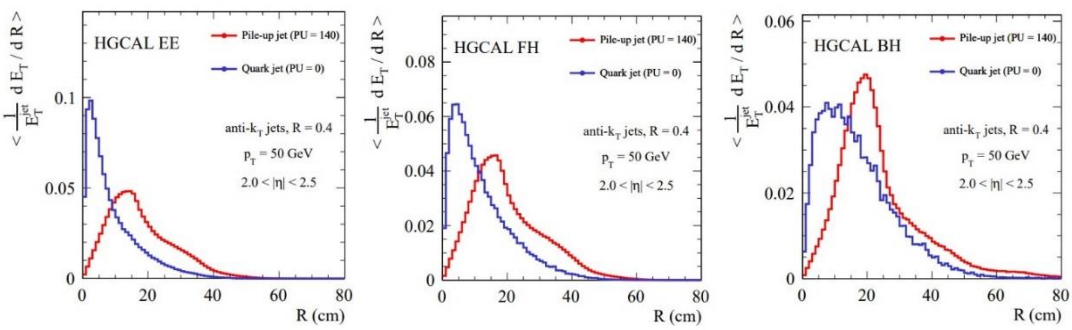

Figure 2.14. The figure presents the radial profile of two types of jets: quark jets (shown in blue) and jets made from PU (shown in red). The radial profile is a representation of the energy distribution of these jets in different layers of the calorimeter. (CMS Collaboration, 2018, The Phase-2 Upgrade of the CMS endcap calorimeter. Technical Design Report, CMS-TDR-019)

In the middle plot, we have the radial profile for the first 12 layers of the FH of the calorimeter. Again, the blue histogram corresponds to quark jets, while the red histogram shows the energy distribution for PU jets.

Finally, in the right plot, we observe the radial profile for the last 12 layers of the hadronic section (BH) of the calorimeter. Once more, the blue histogram represents quark jets, and the red histogram represents jets arising from PU interactions.

The radial profile provides valuable insights into how the energy is distributed in different layers of the calorimeter for both quark jets and jets from PU. It helps us understand the behavior and characteristics of these jets in different parts of the detector.

In Figure 2.15, the comparison is made between the transverse energy fractions contained in different-sized areas for two types of jets: quark jets and jets resulting from PU interactions. On the left side, it shows the distribution of transverse energy within various distances from the center of quark jets with different transverse momenta p_T in a scenario without PU.

On the right side, the plot compares the transverse energy fraction between quark jets and jets formed from PU interactions. PU jets are jets resulting from additional proton-proton interactions within the same bunch crossing. The plot helps us understand how the transverse energy fraction varies with distance for both quark jets and jets caused by PU effects.

By studying these transverse energy fractions and their dependence on distance (ΔR), we gain insights into the energy distribution across jets and the differences between quark jets and jets from PU interactions.

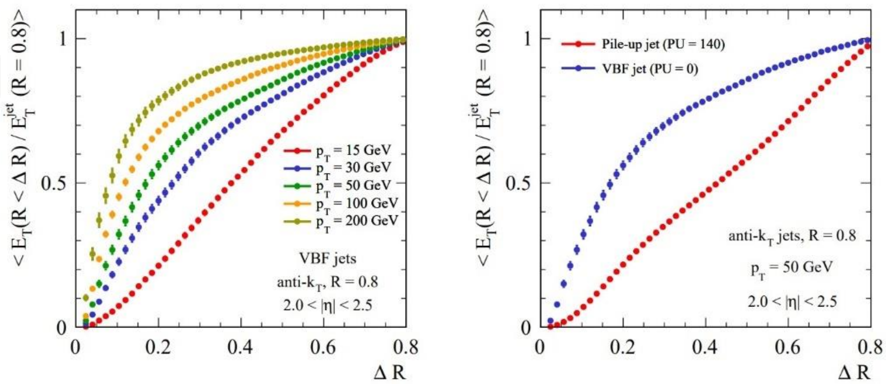

Figure 2.15. The transverse energy fraction at different distances, labeled as ΔR (CMS collaboration, 2018, The Phase-2 Upgrade of the CMS endcap calorimeter. Technical Design Report, CMS-TDR-019)

The anti - k_T algorithm is employed for reconstructing the jets, employing a variable distance parameter (R = 0.8). In the left plot, the transverse energy fraction is shown for different p_T of quark jets. In the right plot, a specific case of quark jets (p_T= 50 GeV, 2.0 < |η| < 2.5) is compared to jets originating from PU interactions.

The plots in Figure 2.13 and Figure 2.15 provide valuable insights into the transverse energy fraction changes concerning the area size for both quark jets and jets resulting from PU interactions.

Based on these observations, goal is to determine an optimal distance parameter that yields the best energy resolution for the jets. This involves finding a balance between the resolution loss due to the inclusion of PU energy and the loss of energy outside the region. Moreover, the optimal distance parameter may vary across different layers of the calorimeter.

The high granularity of the HGCAL allows for a dynamic definition of the jet axis and the parameter "R" (jet size) to be adapted to the specific characteristics of each measured jet. However, no specific optimization or detailed use of the available longitudinal and lateral information has been done yet. It is observed that an efficiency of 80% can yield a rate of approximately 10 kHz for the PU jets. These results demonstrate the possibilities of the HGCAL for jet selection and use all its layers in the analysis.

2.6. Jet performance

Jets in experiments within the field of particle physics, such as those generated at the LHC, result from the remnants of quarks and gluons generated during high-energy processes, examples include parton scattering within colliding protons. It is crucial to understand the resolution of the transverse momentum p_T and the energy scale of jets accurately to estimate systematic uncertainties in various analyses. Jet energy corrections (JEC) are used to adjust and standardize the energy measurements of jets.

The reconstruction of jets involves clustering the four-momentum vectors of particles using the PF algorithm and realistic SimClusters. The anti-k_T algorithm with a radius parameter $R = \sqrt{(\Delta\varphi)^2 + (\Delta\eta)^2} = 0.4$ in the (η, φ) space is used for this purpose. It should be noted that the PF algorithm parameters have not yet been fully optimized for the HGCAL.

2.6.1. PU Jets

PU interactions can cause particles from different events to be mistakenly grouped together, resulting in overlapping low p_T jets that collectively form a single high-p_T jet. These are known as PU jets. We measure the rate of these PU jets by comparing the average number of jets in a specific p_T range to the average number of reconstructed jets that match with particle-level jets. Figure 2.16. illustrates the frequency of PU jets in relation to the quantity of PU interactions. (left) and the PU density (right) for the PUPPI jets. The rate of PU jets in the region where $1.3 < |\eta| < 3.0$ is somewhat lower when compared to the central barrel region of the detector.

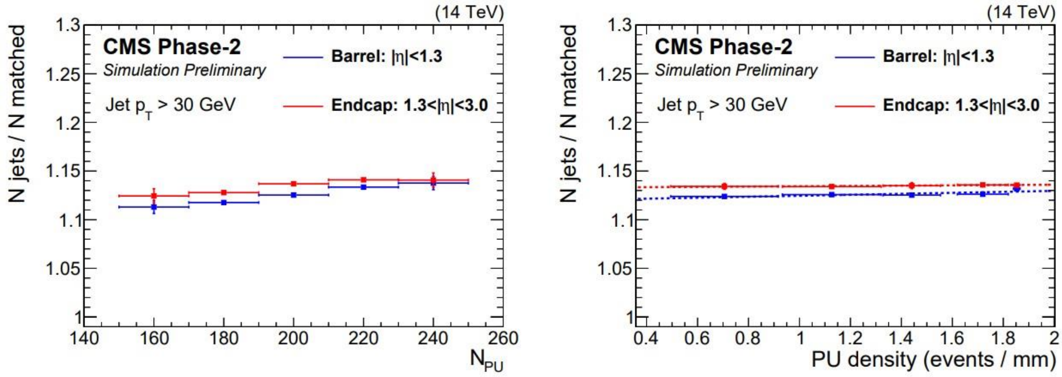

Figure 2.16. The ratio of reconstructed PUPPI jets to reconstructed PUPPI jets matched to particle-level jets from the hard scatter. On the left plot, the ratio is shown as it changes in relation to the number of PU interactions , while on the right plot, it is shown as a function of the PU density. These measurements are specifically for jets with P_T greater than 30 GeV. (CMS collaboration, 2018, The Phase-2 Upgrade of the CMS endcap calorimeter. Technical Design Report, CMS-TDR-019)

3. MATERIAL AND METHOD

In high-energy particle collisions, many new particles are created. One significant outcome of these collisions is the formation of jets, primarily composed of quarks and gluons. This process of jet formation arises from hadronization, where quarks and gluons combine to create color-neutral hadrons. These hadrons subsequently decay into more stable particles that can be detected by particle detectors. Researchers can then study the properties and interactions of these particles in these collisions.

In a CMS analysis, the graphs of PFJet p_T , PFJet η, and PFJet φ show various distributions related to the properties of PF jets reconstructed in the CMS detector. These distributions are essential for understanding the kinematics and characteristics of the jets produced in high-energy collisions, such as those at the LHC. The Data recorded PFJet p_T, η, and φ value of distribution in CMS experiment in 2017 is shown in Figure 3.1.

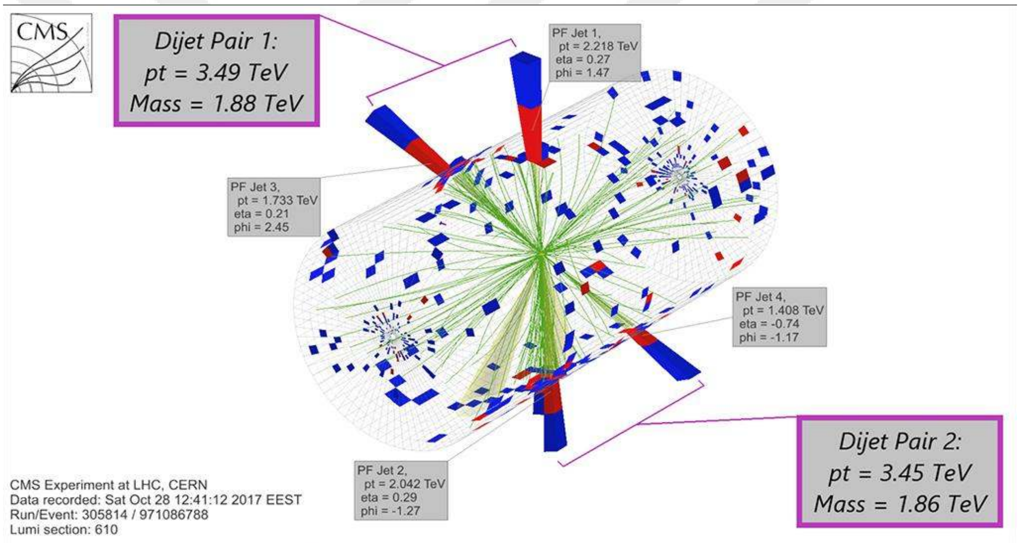

Figure 3.1. Data recorded PFJet p_T , η, and φ value of distribution in CMS experiment.
(https://cds.cern.ch/record/2637847 [last access date: 24.08.2023])

PFJet p_T Distribution:

The graph of PFJet p_T shows the distribution p_T of PFJets in the CMS detector. It represents the momentum of the jets in the plane perpendicular to the beam direction. In other words, it characterizes how much a particle is moving sideways with respect to the direction of the collision.

In the analysis part of my thesis the x-axis of the graphs represents the p_T values in GeV and the y -axis represents the number of jets or the event yield at each p_T. As shown in Figure 4.1-a.

The shape of the distribution can reveal information about the energies of the jets produced in the collisions. High jet p_T values indicate that the jet is moving at high speed perpendicular to the beam axis, while low p_T values indicate slower or less energetic jets.

Mathematically, p_T of a particle is given by the magnitude of its momentum vector in the transverse plane. It is defined as:

$$P_T = \sqrt{(P_x)^2 + (P_y)^2} \tag{3.1}$$

PFJet η (Pseudorapidity) Distribution:

The graph of PFJet η shows the distribution of η of PFJets in the CMS detector. η is dimensionless quantity used to describe the angle of a particle with respect to the beam axis.

The x-axis of the graph represents η values, and the y-axis represents the number of jets or the event yield at each η value (Figure 4.1-b). The η distribution provides information about the angular distribution of the jets and helps in understanding their spatial distribution in the detector. It is defined as:

$$\eta = -\ln\left[\tan\frac{\theta}{2}\right] \tag{3.2}$$

where θ is the polar angle with respect to the beam axis. The range of η spans from negative infinity to positive infinity, with the central region close to $\eta = 0$ and the forward regions at higher absolute values of η.

The η distribution of PFJet is crucial for background estimation, as well as for understanding the kinematic characteristics of various physics processes. It also aids in the optimization of event selection criteria and is essential for precise measurements of SM processes and searches for new physics phenomena.

PFJet φ (Azimuthal Angle) Distribution:

The graph of PFJet φ shows the distribution of the φ of PFJets in the CMS detector. It is the angle in the plane perpendicular to the beam axis, defining the position of the jet around the beam axis. The x-axis of the graph represents φ values, and the y-axis represents the number of jets or the event yield at each φ value (Figure 4.1-c). The φ distribution gives insights into the jet's orientation around the beam axis.

By analyzing these distributions, the behavior of jets produced in CMS collisions can be studied. The patterns can be looked, peak values are identified, and the distributions for different collision energies or types of particles are compared. These analyses contribute to a better understanding of particle physics processes and can help in validating theoretical models and simulations.

Typically, these distributions by filling histograms for each of the PFJet p_T, PFJet η, and PFJet φ variables using the data analysis can be created. The histograms are then plotted to generate the corresponding graphs, which are then analyzed and interpreted to draw conclusions about the properties of the jets produced in the CMS detector.

The CMS experiment employs the PF technique to accurately reconstruct light quark jets produced in high-energy collisions. The PF algorithm plays a vital role in combining information from different sub-detectors to obtain precise measurements of particles' momenta and energies. The process of reconstructing light quark jets with the PF technique involves several key steps:

1. Track Reconstruction: The PF algorithm starts by identifying tracks in the inner tracker of CMS. These tracks represent the paths taken by charged particles as they traverse through the detector. By analyzing the bending of these tracks due to the strong magnetic field, we can determine the momenta and charges of charged particles.
2. Calorimeter Clustering: Next, the PF algorithm looks for energy deposits in the calorimeters, including the ECAL and the HCAL. Photons and electrons primarily release their energy in the ECAL, whereas charged and neutral hadrons distribute their energy between the ECAL and HCAL.
3. Particle Identification: The PF algorithm utilizes the data collected from both tracker and calorimeter the to identify different types of particles. To reconstruct light quark jets, we focus on identifying clusters of energy deposits in the calorimeters consistent with charged and neutral hadrons. These clusters are then linked to the corresponding tracks identified in the tracker.
4. Jet Clustering: After identifying individual particles, the PF algorithm groups them together to form jets. Light quark jets are collimated showers of particles produced by quarks or gluons. To combine the individual particles into jets, we employ algorithms for clustering, , such as the anti-k_T algorithm.
5. Jet Energy Corrections: The final step involves applying energy corrections to the PFJet to account for various detector effects and to calibrate the energy scale. These corrections are essential to ensure that the measured energy of the jet precisely captures the energy of the original light quark that produced it.

By employing the PF technique, we can achieve high precision and efficiency in reconstructing light quark jets in the CMS experiment. This method is crucial for studying the properties of quarks, measuring their energies and momenta, and exploring new physics phenomena involving quarks in the collisions at the LHC.

In the particle physics experiments, such as those conducted at large colliders like the LHC, Generated jets (GENJets) refer to the jets that are obtained from computer simulations known as MC simulations. In these simulations, scientists use theoretical models based on the fundamental laws of physics to predict how particles will behave in high-energy collisions. The simulations generate initial particles, such as quarks and gluons, and follow their interactions and decays as they travel through a simulated detector. As these particles interact and decay, they produce collimated showers of particles known as jets. The jets obtained directly from this simulated process are referred to as GENJet.

GENJet serve as a valuable reference for comparison with the jets reconstructed from real experimental data. By comparing the properties of reconstructed jets (obtained from actual detector data) to those of GENJets (obtained from MC simulations), we can assess how well the reconstruction algorithms reproduce the true properties of the particles.

GENJets play a crucial role in evaluating the performance of jet reconstruction algorithms and improving our understanding of the particle interactions observed in high-energy collisions. They are an essential tool in the quest to unravel the mysteries of the subatomic world and gain insights into the fundamental constituents of the universe.

GENJets are obtained from MC simulations and serve as a reference for comparison, while PFJet are reconstructed from real detector data using the PF technique and are used in physics analyses. The comparison between GENJets and PFJet helps validate the performance of the detector and provides a deeper understanding of the particles produced in high-energy collisions.

3.1. Reconstruction of PFJet

In this thesis, the performance of jets in a specific type of collision called QCD event is evaluated. Jets are groups of particles produced in these collisions that share common properties. To reconstruct the jets, a special algorithm called the anti-k_T algorithm is used, which helps to identify and group the particles together.

There are three types of jets: PFJets, Calorimeter jets (CaloJets), and Reference (RefJets). PFJets are constructed by integrating data from each of the subdetectors of the detector. CaloJets, on the other hand, are formed using the energy deposited in specific parts of the detector. RefJets are created using only stable particles produced in the event, excluding neutrinos.

We are studying PFJet with a minimum p_T of 15 GeV, which means we are looking at jets with a certain level of energy and momentum. For CaloJets, we only consider those with p_T higher than 20 GeV, as lower values are not as reliable for our analysis.

By comparing the performance of these different types of jets, we can better understand how well our detector is working and how accurately we can identify and measure the particles produced in these multijet events. This information helps us improve our analysis techniques and gain valuable insights into the behavior of particles in high-energy collisions.

Figure 3.2 describe the p_T of each PFJet is compared to the p_T of the corresponding jets obtained from the generated RefJets and the CaloJets energy deposits. The four-momentum of each jet is calculated by adding up the four-momentum vectors of its individual constituents., without applying any jet energy corrections.

This comparison allows us to assess the efficacy of the PF jet reconstruction process in reproducing the p_T of the jets originating from particle generation and those reconstructed in the calorimeter. It helps evaluate the accuracy of the jet reconstruction algorithm and its ability to measure the energy and momentum of the particles accurately in dijet events.

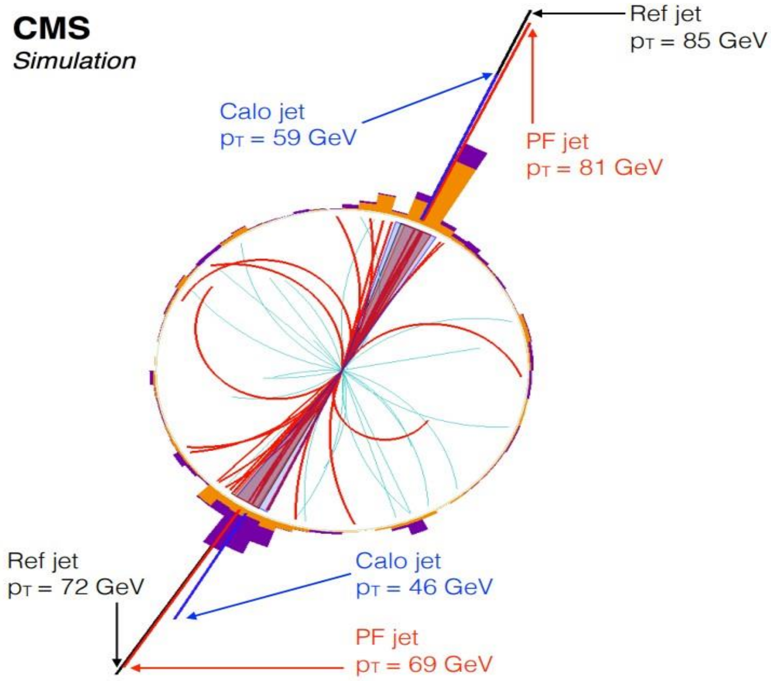

Figure 3.2. In this simulated dijet event, process of jet reconstruction is executed utilizing the PF algorithm.. The particles are clustered to form two PF jets, which are shown with thicker lines in the diagram. Particles p_T less than 1 GeV are not displayed for clarity (The CMS Collaboration, 2017, PF reconstruction and global event description with the CMS detector. CMS-PRF-14-001, Journal of Instrumentation, DOI 10.1088/1748-0221/12/10/P10003)

3.1.1. Jet Clustering

In particle physics experiments, jet algorithms are commonly grouped into two primary classes: cone-based algorithms and sequential recombination algorithms. Cone algorithms group particles within a fixed distance in the η-φ plane, forming jets around the center. On the other hand, sequential recombination algorithms calculate variable distances between particle pairs based on their p_T , avoiding a fixed geometric shape for the jets. Jet clustering algorithms can be classified as collinear safe or infrared safe. Collinear safe algorithms are not affected by splitting an input particle into two collinear particles, while infrared safe algorithms remain unchanged when adding soft particles. Modern high-energy physics experiments prefer infrared and collinear safe sequential recombination algorithms over collinear and infrared unsafe ones.

At CMS, the anti- k_T algorithm is the default jet clustering algorithm. It is favored because it is both collinear and infrared safe, making it suitable for perturbative QCD calculations and efficient in the CMS experiment.

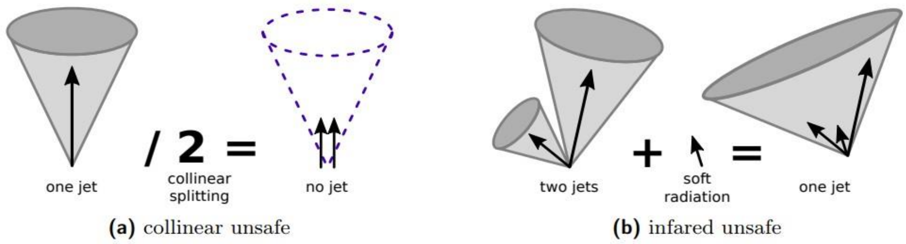

Figure 3.3. An instance of a jet clustering algorithm that is susceptible to collinear and infrared effects is the "fixed-cone" algorithm. In this algorithm, particles within a predetermined distance in the η-φ plane are grouped to create jets. Nonetheless, if the constituent particles' momenta fall below a specific threshold, the algorithm does not reconstruct a jet. This attribute renders it collinear unsafe. (Andrieu, B., 2004. Jet finding Algorithms at Tevatron. DO collaboration, LPNHE, Paris)

3.1.2. anti- k_T algorithm

Jet clustering algorithms are essential tools for studying particle collisions. Different algorithms have been debated for their advantages in defining jet boundaries. Some algorithms have regular boundaries, while others are more adaptable to soft radiation. Recent developments allow for analytical calculations to compare the properties of jet boundaries in various algorithms. One interesting finding is that all known safe algorithms can still have irregular boundaries due to soft radiation. The debate continues on whether regular or less regular boundaries are better. Regular boundaries provide rigidity in adapting jets to radiation, while less regular boundaries allow for more flexibility. Both methods have their advantages and disadvantages for experimental calibration and theoretical calculations. An example of a jet algorithm with a soft-resilient boundary is the "iterative cone" algorithm used in some experiments. It iteratively looks for stable cones to define jets, but it may have limitations when dealing with collinear processes.

A simplified explanation of the anti- k_T algorithm can be written as below:

1. Initialization: each particle in the event is treated as an individual "*proto-jet*" or "*seed jet*." Each particle is assigned a distance parameter, which quantifies how close it is to other particles in terms of their k_T and angular separation ΔR. The distance parameter is then used to determine which particles should be merged together to form jets.

During the initialization step, each particle is considered a "*seed*" for a potential jet. The algorithm then calculates the distance between every pair of particles and identifies the smallest distance. If this smallest distance is a distance between two particles d_{ij}, it means that these particles are close enough to be merged together into a single jet. If the smallest distance is a distance between a particle and the beam d_{iB}, it means that this particle should be considered an individual jet.

By repeating this process and re-calculating the distances after each merging, the algorithm gradually groups particles together continue this process until all particles are assembled into jets. The choice of distance parameters and the iterative clustering process are designed to produce well-separated and well-defined jets from the initial particle seeds. This helps in reconstructing hadronic activity and identifying high-energy jets in particle collisions.

2. Calculating distances: For each pair of particles i and j, we calculate the distance between them as d_{ij}, and distances between entities and the beam, denoted as d_{iB}.

$$d_{ij} = \min\left(k_{ti}^{2p}, k_{tj}^{2p}\right)\frac{\Delta R_{ij}^2}{R^2}$$

$$d_{iB} = k_{ti}^{2p}$$

where

$$\Delta R_{ij}^2 = \left(\eta_i - \eta_j\right)^2 - \left(\varphi_i - \varphi_j\right)^2$$

We have three important properties of particle i: its transverse momentum (k_{ti}), rapidity (η_i), and azimuth (φ_i). Additionally, we have introduced two parameters: the radius parameter R in the η-φ space. The R controls the size of the jets, while the p governs the relative importance of the energy versus geometrical scales. These parameters play a crucial role in the jet clustering algorithm, determining how particles are grouped together to form jets based on their momenta and positions in the detector.

3. Finding the smallest distance: We start by identifying the smallest distance among all these distances.
4. Merge or form a jet: If the smallest distance is a d_{ij}, we combine the corresponding entities i and j to make single newly jet. If the shortest distance is d_{iB}, we consider parameter i as a final jet and remove it from the list.
5. Recalculate distances: After forming a jet or removing a particle, we recalculate the distances between the newly formed jets and the remaining particles.
6. Repeat: Then, we repeat the procedure until all entities have been clustered into jets. This inclusive clustering approach helps us organize the particles or pseudojets into jets based on their proximity.

The anti-k_T algorithm favors the clustering of soft and collinear particles around higher-p_T seed particles, resulting in relatively round and well-separated jets. It is particularly useful for identifyin high-energy jets and reconstructing the hadronic activity produced in particle collisions.

3.2. Monte-Carlo Simulation for jets

In the research of particle physics, the simulation of both the hard process and the interactions of particles with the detector holds paramount significance in the comparison of theoretical predictions with experimental measurements. To achieve this, the technique of MC simulations is employed. These simulations generate numerous random events that represent interaction processes, yielding numerical descriptions of anticipated measurement outcomes. Given that many processes elude direct calculation using QCD, approximations become necessary. Perturbative QCD adopts a factorization strategy to derive quantitative predictions based on the concept of asymptotic freedom. This entails expressing observables, like the cross-section of hard interaction processes, as functions of the strong coupling constant αs for a specific scale Q. The initial contribution is termed Leading-Order , followed by Next-To-Leading-Order , and so forth. The use of such simulations facilitates the investigation of specific physics processes by diminishing the number of required simulated hard interactions, rendering the analysis more manageable and illuminating.

To contrast the MC simulation with actual data acquired from intricate detectors, a detector simulation is layered atop the aforementioned stages. This simulation accommodates the interaction between particles and the detector's material, utilizing a three-dimensional model of all detector components. This endeavor elucidates how the detector influences particles and responds within the MC simulation. In the context of particle physics analyses, distinctive insights materialize at different stages of the MC simulation. The parton-level encapsulates the end products of the hard process. Progressing to the particle-level incorporates the inclusion of hadronized parton showers. Finally, at the detector-level, the detector simulation is employed to reconstruct the signatures of particles. This progression enables us to meticulously trace the trajectory of an individual quark or gluon from its inception to its eventual detection within the detector.

By scrutinizing each step in isolation, we can unravel the impact of distinct effects, a pivotal process in calibrating jets and refining our grasp of the fundamental physics at play.

3.2.1. Hard Scattering Event Generation

In the first step, the event generator generates the primary proton-proton collisions which both soft elastic interactions and hard inelastic scattering occur. Understanding the physics at high-energy hadron colliders like the LHC requires knowledge of QCD. According to the parton model, quarks and gluons are bounded inside proton, which are called partons toghether. When protons collide, it is, in fact, a collision between their constituent partons. These partons are characterized by parton distribution functions, and depend on the proportion of momentum of the partons inside the proton and the scale of energy Q^2 uses to investigate the proton. Perturbative calculations are applicable at high center-of-mass energies where the strong coupling constant α_s is small, allowing for a description of the collision between the incoming protons. The factorization theorem is used to predict the characteristics of the hard-scattering interactions, enabling the determination of the total hadronic cross section.

$$\sigma_{p+p} = \int_0^1 dx_1 \int_0^1 dx_2\, f_1^p(x_{1,}Q^2) f_2^p(x_{2,}Q^2) \sigma_{1+2\to X} \quad (3.3)$$

Therefore, to calculate the total rate for a hard scattering interaction, we focus on determining the sub-process cross section $\sigma_{1+2\to X}$. This involves identifying the leading-order partonic processes that contribute to the collision of particles 1 and 2, resulting in the production of X.

3.2.2. Detector Simulation

The simulated jets are then propagated through the detector model, accounting for interactions with the detector material and detector response. This step allows the simulation to mimic the experimental response and reconstruction of jets in the actual detector.

In this thesis , MC sample for all test beams was generated using a GEANT 4 simulation based on CMSSW[3].GEANT 4 is a powerful tool used to simulate the interaction of particles produced in collisions involving protons within the CMS detector. This simulation includes the interactions of particles with the diverse parts of the detector, such as the tracker, muon chambers, electromagnetic and hadronic calorimeters. GEANT 4 considers the various physics interactions occurring during particle propagation, such as energy loss, scattering, and particle decays, to accurately model the behavior of particles as they traverse through the detector material. This allows researchers to study and analyze particle interactions and their behavior within the experimental setup.

By combining all these steps, the MC simulation provides a prediction of the properties of jets, such as their energies, momenta and angular distribution.

MC simulations are crucial for understanding the backgrounds, estimating the detector efficiency, and interpreting experimental data in high-energy physics experiments. They are also used to compare experimental measurements with theoretical predictions, enabling the validation of the SM and the search for new physics beyond it.

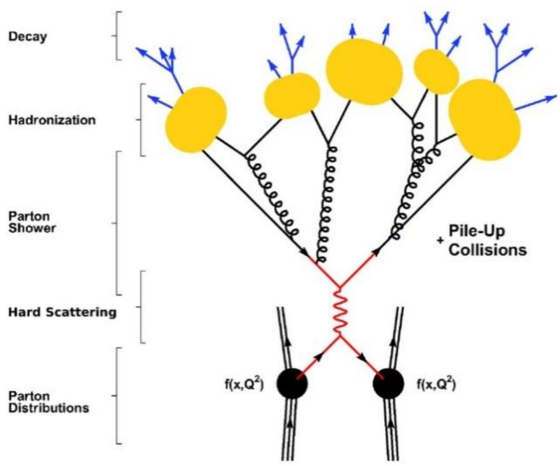

Figure 3.4. Illustration of the event generation chain in proton-proton collisions (Bauer, J, 2010, Prospects for the Observation of Electroweak Top-Quark Production with the CMS Experiment, PhD thesis, Karlsruher Institut f¨ur Technologie, Karlsruhe, 156 p)

4. RESULTS AND DISCUSSIONS

In this thesis, analysis performed using the HGCAL which will be future endcap calorimeter of the CMS experiment. The study focuses on assessing the accuracy and precision of the HGCAL. To achieve this, the responses of the HGCAL are evaluated using simulated data collected from proton-proton collisions at a center-of-mass energy of 14 TeV. An EDM (Event Data Model) analyzer code in the CMS experiment is used. EDM is a data format used in the CMS experiment to store information about the event data recorded during collisions in the LHC.

Through this code an ntuple (a ROOT TTree) for the study of HGCAL clusters and tracksters is created. This analyzer reads data from various collections (CaloClusters, CaloParticles, Tracksters, GenParticles, PFJet) using tokens. The data read from these collections is used to fill the TTree with information about the events and various reconstructed quantities (energies, positions, time). The analyzer uses mathematical vectors (ROOT::Math::PxPyPzEVector, ROOT::Math::XYZPointF, ROOT::Math::XYZVector, etc.) to store 4-vectors and 3D positions of objects.

4.1. Flat p_T sample

The analyzer code for p_T sample is written to configure a CMS software framework for geometry of the HGCAL in the context of the Phase 2 upgrade, version C11I13M9 of the CMS detector.

For beginning reports of PFJets were obtained for *up quark* and then for the *down quark* and *gluon* jets. After analyzing different p_T bins, a flat p_T sample for 14 TeV was generated. The purpose of generating this flat p_T sample is likely to have a uniform and broad representation of jets at different momentum scales. Such samples are useful for understanding the response of the detector to different energy deposits and for calibrating the jet reconstruction algorithms across a wide p_T range.

The Figure 4.1.a represents the PFJet graph that illustrates the variation in jet p_T at different energy levels within our sample. This graph provides a comprehensive view of how p_T of jets evolves across a spectrum of energy regimes, shedding light on the dynamic behavior of particles within our studied interactions.

In the Figure 4.1.b the distribution of PFJet η is presented obtained from analysis. As part of our investigative objectives centered on the analysis of jets derived from the HGCAL region, we implemented a selection criterion by restricting the η to the interval of 1.8 to 2.1. This constraint was imposed in order to focus our study exclusively on events characterized by jets originating within the specified η range, thereby refining the scope of our investigation.

This information is essential for understanding particle production in the forward direction and for studying physics processes that involve particles produced at high rapidity.

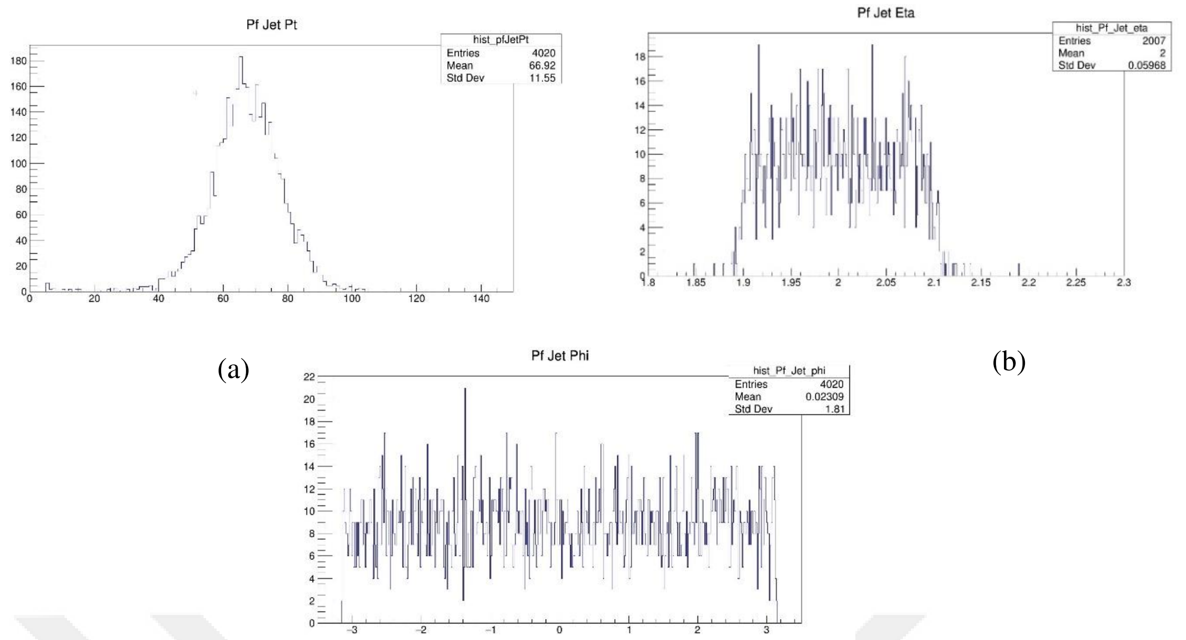

(a) (b)

(c)

Figure 4.1. Result from HGCAL analysis event generated for 2000 event, no pile up sample, |η| < 2and the events are further filtered based on the condition that the p_T of the particles is 100 GeV (GeV/c).

The shape of the η distribution is influenced by various factors, including PDFs of the colliding protons, the initial state radiation, and the detector acceptance. Detailed comparisons with theoretical predictions and MC simulations are performed to validate these results and calibrate the jet reconstruction performance in different η regions.

In Figure 4.1.c the PFJet φ graph obtained from analysis in the HGCAL is shown. The azimuthal distribution of PFJet is a key aspect of analysis, providing essential information about the angular distribution of jets within the CMS detector. In this section, the φ distribution of PFJet obtained is presented, focusing on the range from -3 to +3.

In the CMS coordinate system, the φ angle is measured in the plane perpendicular to the beamline. It spans the range from -φ to +φ corresponding to -3 to +3 in the units we are using.

This analysis reveals a symmetric φ distribution, as expected due to the cylindrical symmetry of the CMS detector. The φ distribution of PFJet shows a uniform spread of jets around the detector's central axis. This uniformity is crucial for our understanding of the detector's response and ensures that the jet reconstruction is well-calibrated throughout the entire φ range.

The observed φ distribution is in excellent agreement with theoretical predictions and MC simulations, validating the accuracy of our jet reconstruction algorithms in capturing φ of particles. Additionally, this distribution helps us optimize the reconstruction performance and correct for any potential detector effects that may introduce φ dependent biases.

These results were discussed and confirmed by TTU HGC DPG group meeting that has been being held between Texas University, Çukurova University, and CERN.

4.2. QCD sample

Subsequently, the QCD event samples were generated for geometry Extended2026D77, which is relevant to the Phase-2 upgrade of the CMS detector. The simulation process is related to QCD events with a p_T range of 600 to 800 GeV at a center-of-mass energy of 13 TeV. The process involves creating GEN events and then simulating them. The maximum number of events to be processed in the simulation is set to 1000. The events are being generated and processed with specific conditions (phase2_realistic_T21) and a global tag. The Pythia8 generator is being used with specific settings defined in the 'pythia8CommonSettings' and 'pythia8CUEP8M1Settings' parameter sets. p_T, η, ϕ and other particular branches added to ntuple from the ak4 PFJet collection. And new results with p_T, η, and ϕ's distributions were obtained and compared with previous results.

Figure 4.2.a. represents the distribution of PFJet, using a QCD sample. Goal was to examine the behavior of the PFJet p_T values and understand their distribution characteristics. The p_T range of 0 to 150, the number of events decreased significantly from 10^6 to 10^3. Subsequently, in the range of 150 to 300, a decreasing trend in the number of events was still apparent, albeit with some fluctuations. Notably, within this range, there were intervals where the number of events appeared to remain relatively stable. This observation suggests that the production rate of PFJet decreases as their p_T increases. However, in the higher p_T region (150 to300), there may be some factors contributing to fluctuations in the event count, and the overall trend of decreasing jet production seems to persist. The stability of the event count in certain intervals within this range could be indicative of specific physical processes or selection effects.

Figure 4.2.b η distribution of PF jets obtained from QCD sample is shown. The plot exhibited a distribution of PFJet η values that showed intriguing features. The number of events y -axis increased steeply from 0 up to approximately 10^4 events between -5.5 and -5 on the x-axis. Beyond this point, the event counts continued to increase until approximately 10^5 events and experienced a slight rise until the -3 region of the x -axis. This region corresponds to the forward region in the detector. The plateau-like behavior with fluctuations was observed between -3 and +3 on the x-axis, indicating a stable response of the detector in this central region. After +3 on the x-axis, the number of events began to decrease gradually until approximately 10^4 events until the +5 region. This region corresponds to the backward region in the detector. Between +5 and +5.5 on the x-axis, the event count decreased steeply to 0. The observed steep increases and decreases in event counts are symmetrical with respect to the central region (around 0 on the x-axis). The similar behavior suggests that the detector is symmetrically responsive to PFJet in both forward and backward directions. The plateau-like behavior observed between -3 and +3 on the x-axis indicates a saturation effect in the PFJet η distribution. The decreasing trend in event counts beyond -3 and +3 on the x-axis might be related to the decrease in detector efficiency or acceptance in the extreme regions.

Figure 4.2.c represent the φ distribution of PF jets. The main goal was to understand the characteristics of PFJet φ values and their distribution. The plot revealed a distribution of PFJet φ values that exhibited intriguing patterns. The distribution resembled a Gaussian-like shape, with the φ values concentrated around the center of the distribution, resembling a bell-shaped curve. In the plot, the number of events y-axis increased steeply from 0 to approximately 10^5 events betwee 3.5 and -3 of the x-axis. This region represents the forward direction in the detector. Beyond this point, the event counts plateaued and did not change significantly, with only slight fluctuations observed between -3 to +3 radians of the x-axis. The plateau was maintained at a value slightly above 10^5 events. Hocam bu sekiller yeni elde edildi ve eklendi

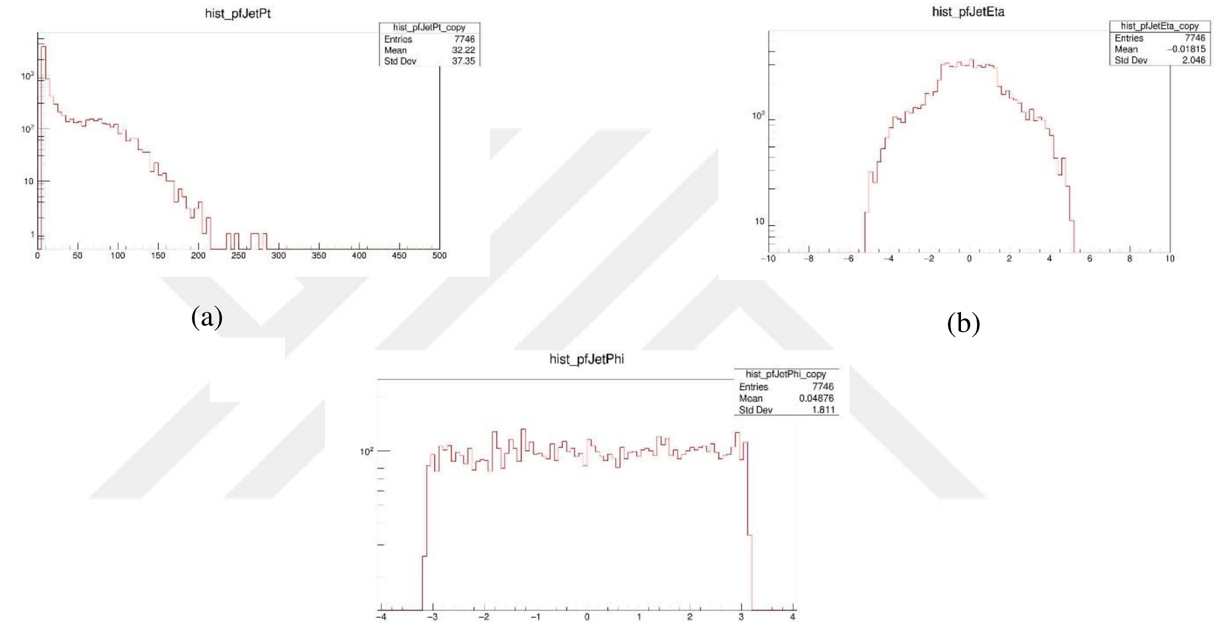

(c)

Figure 4.2. Results with p_T, η, and ϕ's distributions obtained from the simulation process is related to QCD.

After the plateau region, the event counts slightly decreased as the ϕ increased further from +3 to +3.5 radians. This region corresponds to the backward direction in the detector. The observation of similar event counts after the plateau region (between -3 and 3) suggests that the detector exhibits a stable and consistent response in this central region. The plateau-like behavior, with the event counts remaining almost constant, indicates a saturation effect in the PFJet ϕ distribution.

The saturation effect may be related to the detector geometry, acceptance limits, or specific physics processes. It is important to study the reasons behind this behavior to understand the detector's performance and its implications for physics analyses. To achieve a comprehensive understanding of the PFJet distributions, further analyses were performed, including comparisons with gen jet particles. This comparison provided valuable insights into the agreement between PFJet and their corresponding generated GENJet particles. Understanding this agreement is essential in validating the detector response and improving the accuracy of physics analyses.

4.3. The performance of the GENJets and PFJet in HGCAL

Comparing the properties of reconstructed jets such as PFJet with GENJets is a crucial step in validating the simulation and detector response. It helps to assess the accuracy of the reconstruction algorithms and the energy calibration of the detector. In a typical QCD sample simulation, the MC generator simulates the hard scattering process involving partons like quarks and gluons from the colliding protons. These partons undergo various interactions and fragmentation processes, leading to the production of final-state particles, including jets.

GENJets are clusters of particles produced during the simulation that represent the final-state manifestation of the quarks and gluons from the initial hard scattering. These GENJets can be analyzed in the same way as reconstructed jets from simulated data to study the properties of the underlying QCD processes and validate the performance of the detector.

Figure 4.3 describes p_T distribution PF jets and their corresponding GENJets in a QCD sample.

The p_T values for both PFJet and GENJet were plotted, and the resulting graph ranged from 0 to 300 GeV. In the lower p_T region, the event counts for both PFJet and GENJet reached approximately 10^6, with GENJets p_T being slightly higher than PFJet p_T. This observation suggests a good agreement between the two distributions at lower values.

As p_T increased, both PFJet and GENJet exhibited a gradual decrease in event counts. Between 0 and 50 GeV, the decrease was uniform for both, with the event counts remaining similar. This region indicates that PFJet and GENJet have comparable pt distributions in this intermediate range.

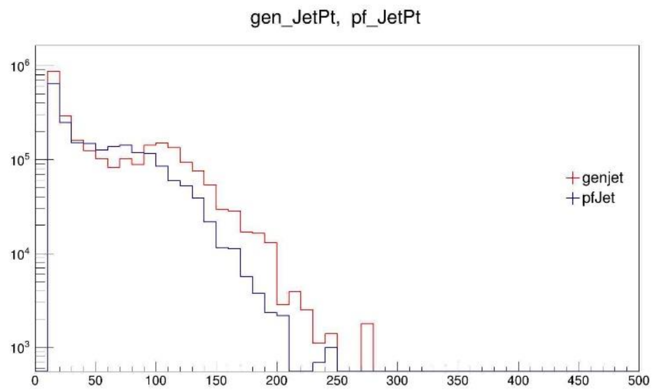

Figure 4.3. Comparison between PFJet p_T and genJet p_T in the QCD sample.

Between 50 and 100 GeV, a noticeable change occurred, with the event counts for PFJet being slightly higher than those for GENJet. This discrepancy might indicate variations in the detector response or reconstruction algorithms in this p_T range.

Beyond 100 GeV up to 300 GeV, both PFJet and GENJet continued to decrease in event counts. However, this time, the GENJets p_T event counts were slightly higher than those of PFJet. This region of the distribution indicates that GENJet have a slightly higher representation than PFJet at higher p_T values.

The observed agreement and discrepancies between PFJet and GENJet provide valuable insights into the detector response and the reconstruction of jets in this QCD sample. The good agreement at lower p_T values and discrepancies in specific p_T ranges can guide improvements in the detector calibration and reconstruction algorithms.

η distributions of both GENJets and PFjets in a QCD sample is shown in Figure 4.4. The main aim was to compare the η distributions and understand the agreement between the two types of jets. The plotted distributions of GENJets η and PFJet η exhibited similar patterns. Both distributions showed a steady increase in event counts from 0 up to approximately 10^5 events between -5.5 and 0 on the x-axis. Beyond this, both distributions gradually decreased in event counts from 0 to +5.5. This observation indicates that GENJets and PFJet distributions have similar trends in terms of η.

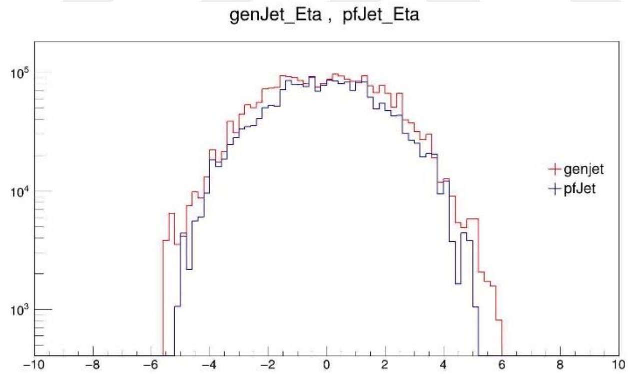

Figure 4.4. Comparison between GENJet η and PF jet η

The φ distributions of both GENJets jets and PFJet in a QCD sample is illustrated in Figure 4.5. The plotted distributions of GENJets φ and PFJet φ exhibited similar patterns. Both distributions were filled between -3.2 and +3.2 on the x-axis, representing the φ range in radians.

Starting from -3.2 and increasing towards -3 on the x-axis, both distributions displayed a steady increase in event counts. Beyond this region, the distributions reached a relatively constant level, with slight fluctuations in event counts observed between -3 and +3 on the x-axis.

An important observation was that the GENJets φ distribution had a higher frequency of events compared to the PFJet φ distribution. This higher frequency indicates that GENJet were detected more frequently in various φ compared to PFJet.

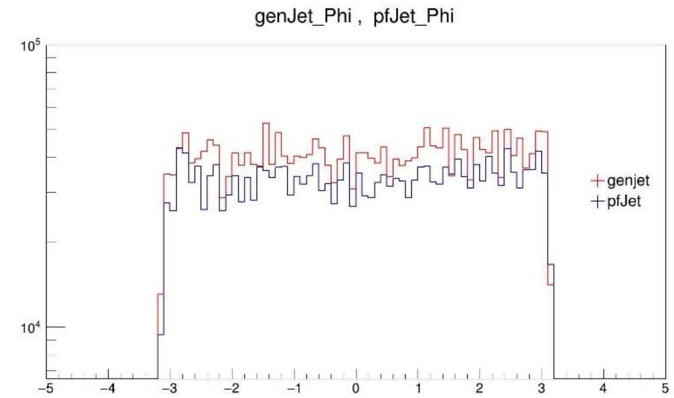

Figure 4.5. Comparison between GENJet φ and PF jet φ

For getting more information about GENJets and PFJet distribution in the next step both sides of HGCAL were chosen in Ntuple, and a new sample was generated, on looking deltaR (minimum distance) between GENJets with the highest p_T to its matched PFJet p_T was calculated and was drawn.

The result taken from analysis is shown in Figure 4.6. The Delta R (ΔR) distribution between the highest p_T GENJet and the highest p_T PFJet in a QCD sample is examined in this analysis. The aim was to study the angular separation between the two types of jets and understand their correlation. Bu şekil yeni eklendi

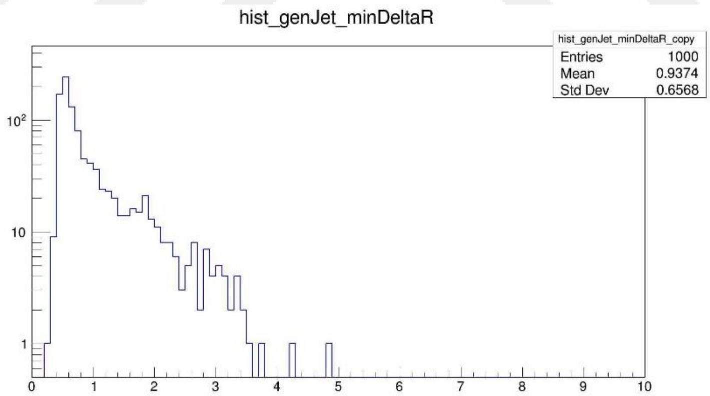

Figure 4.6. The Delta R (ΔR) distribution plot between the highest p_T GENJet and the highest p_T PFJet

The plotted distribution of ΔR ranged from 0 to 10 on the x-axis, representing the angular distance between the highest p_T of GENJets and the highest p_T of PFJet. The y-axis represents the number of events or event counts. It shows the frequency of occurrences where the highest p_T of GENJets and the highest p_T of PFJet have a specific angular separation (ΔR value).

At very small values of ΔR, namely 0.5 and 2 on the x-axis, the distribution showed a limited number of events with a value of 1 on the y-axis. This observation indicates that there were specific cases where the *highest p_T GENJets* and *highest p_T PFJets* were very close together in angular separation, resulting in a small ΔR value.

Beyond ΔR = 2.3 on the x-axis, the distribution started increasing gradually, reaching up to 100 on the y-axis at ΔR = 3.25. This region indicates that the highest p_T GENJets and highest p_T PFJet were generally well separated in their angular positions.

After ΔR = 3.25, the event counts started to decrease, but at a slower rate, until reaching ΔR = 6 on the x-axis. This observation suggests that, at larger ΔR values, the *highest p_T GENJets* and *highest p_T PFJet* were increasingly distant from each other.

At ΔR = 7 on the x-axis, there was another noticeable peak in the distribution, with a value of 1 on the y-axis. This feature indicates that there were specific instances where the *highest p_T GENJets* and *highest p_T PFJet* were exceptionally well-separated with a larger ΔR value.

For further investigation PFJet Multiplicity and Gen Jet Multiplicity is obtained from analysis which is shown in Figure 4.7. The x-axis represents energy scale, and the y-axis represents the values of the jet multiplicities.

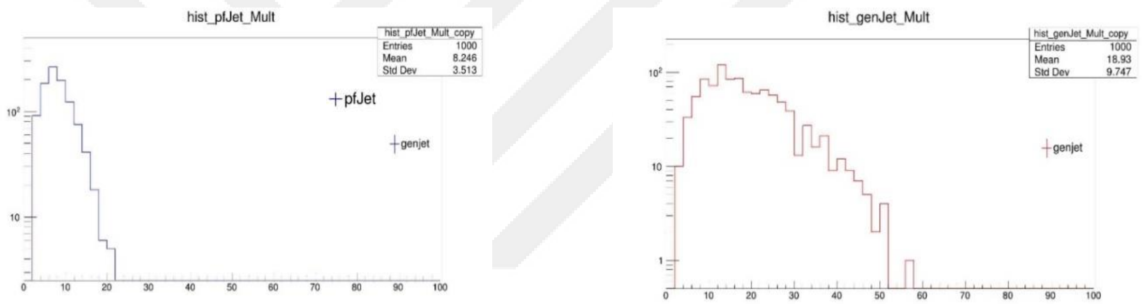

Figure 4.7. Distribution of multiplicity of PFJets and multiplicity of GENJets produced by QCD sample.

PFJet Multiplicity Starts at 0 and increases gradually from 0 to higher than 100. At point 10 on the x-axis, it starts decreasing back to 22 gradually. The increase in PFJet multiplicity suggests that more PFJet are being produced or detected as energy scale increases. The subsequent decrease indicates that the production or detection of PFJet decreases beyond a certain point. This can be due to energy limitations, physical processes, or detector effects.

Gen Jet Multiplicity increases from 0 to a maximum value of 100 at point 10 on the x-axis. This suggests that more GENJets are being produced or detected as energy scale increases, and the process seems to reach its maximum at 100. After reaching the maximum value, the Gen Jet multiplicity starts to decrease gradually, indicating that the production or detection of GENJets decreases beyond point 10. This decrease could be due to the same reasons as mentioned for PFJet.

The analysis yielded analogous results for the down quark as compared to the up quark, with minor distinctions observed between the two. The observed differences, albeit small, were indicative of unique characteristics associated with each quark type within the context of the study.

5. CONCLUSION

The analysis are done to perform a comprehensive comparative study between PFJet and GENJet to validate their mutual consistency. This investigation is motivated by the overarching goal of assessing whether the empirical behavior of these two distinct jet types aligns with theoretical expectations and empirical observations.

The primary objective of this comparison is to confirm that the agreement between PFJet and GENJet, particularly in terms of essential jet properties such as energy, momentum, and angular distributions, conforms to theoretical predictions and experimental calibration. These properties are pivotal in evaluating the concordance between these two categories of jets.

The anticipated outcome, grounded in established theoretical frameworks and prior experimental findings, posits that PFJet and GENJet should demonstrate a substantial degree of coherence. PFJet, being the result of intricate reconstruction processes from detector measurements, offer a practical representation of particle-level jets, while GENJet are theoretically generated, serving as a benchmark for the anticipated behavior of jets without the influence of detector effects.

A positive outcome, wherein PFJet and GENJet exhibit alignment, would affirm the reliability of the particle reconstruction procedures, highlighting the effectiveness of detector calibration and the robustness of the employed algorithms. Such a result would be congruent with prevailing theoretical models and contribute to the broader validation of the experimental methodology.

Our forthcoming research plan entails an expansive extension of the efficiency assessment framework within the HGCAL. This expanded research endeavor necessitates the incorporation of a broader array of parameters and a more intricate analytical methodology.

It is my aspiration that the subsequent stages of my academic journey will offer the opportunity to engage in these advanced research pursuits, thereby facilitating a more comprehensive and detailed exploration of the efficiency characteristics inherent to the HGCAL.

REFERENCES

Andrieu, B., 2004. Jet finding Algorithms at Tevatron. DO collaboration, LPNHE, Paris

Bauer, J, 2010, Prospects for the Observation ofElectroweak Top-Quark Productionwith the CMS Experiment, PhD thesis, Karlsruher Institut f¨ur Technologie, Karlsruhe, p-156

CMS Collaboration , 2018, The Phase-2 Upgrade of the CMS endcap calorimeter, Technical Design Report, CMS-TDR-019.

CMS Collaboration, 2021. CMS Data Acquisition and High Level Trigger Technical Design Report. CERN-LHCC-2021-007, CMS-TDR-022.

CMS Collaboration,2012. Alignment of the CMS silicon tracker. J. Phys.: Conf. Ser. 368 012036

https://cds.cern.ch/record/2797452/files/OverviewDrawing_October2019.png [last access date: 17.10.2023]

https://tr.overleaf.com/learn/latex/Feynman_diagrams [last access date: 20.07.2023])

https://twiki.cern.ch/twiki/pub/CMSPublic [last access date: 24.08.2023]

https://universe-review.ca/I14-03-BBN.jpg [last access date:14.10.2023]

https://www.shutterstock.com/tr/image-vector/electron-positron-annihilation-772129372 [last access date: 20.06.2023

Khattak, G., Vallecorsa, S.,Carminatia, F., and Muhammad Khan, G., 2011. Fast Simulation of a High Granularity Calorimeter by Generative Adversarial Networks. CERN, Geneva , Switzerland.

NASA, 2006. Brief History of the Universe.

Sebastian, M., 2016. Trigger Algorithms and Monte Carlo Event Generation for Dijet Searches in ATLAS and Beyond. Master's Thesis, Friedrich Alexander University, Erlangen, Germany, p-57

Study of quark and gluon jet substructure in Z+jet and dijet events from pp collisions The CMS Collaboration

Walter, P., 2021. Origin and Evolution of the Universe. Journal of Modern Physics, Vol.12 No.13

William, R., 1994.Techniques for Nuclear and Particle Physics Experiments. Springer-Verlag Berlin Heidelberg GmbH, New York, p-378

CURRICULUM VITAE

Personal Information

Last name, First Name : Azimi Zohra

Education

Degree	Kurum	Mezuniyet Yılı
Master	Çukurova Üniversitesi	2023
Bachelor	Kabul University, Afghanistan	2016
High School	Merways Mina , Afghanistan	2013

Work Experiences

Year	Organization	Position
2017-2019	TMV schools	Teacher of Physics